Draft version June 26, 2019, submitted to ApJS at January 31, 2019
Typeset using LaTeX **twocolumn** style in AASTeX62

Electron Capture Supernovae of Super-AGB Stars: Sensitivity on Input Physics

Shing-Chi Leung,[1] Ken'ichi Nomoto,[1] and Tomoharu Suzuki[2]

[1] *Kavli Institute for the Physics and Mathematics of the Universe (WPI), UTIAS, The University of Tokyo, Kashiwa, Chiba 277-8583, Japan*

[2] *College of Engineering, Chubu University, 1200 Matsumoto-cho, Kasugai, Aichi 487-8501, Japan*

(Dated: June 26, 2019)

ABSTRACT

Stars of $\sim$ 8 - 10 $M_\odot$ on the main-sequence form strongly electron-degenerate O+Ne+Mg core and become super-AGB stars. If such an O+Ne+Mg core grows to 1.38 $M_\odot$, electron captures on ^{20}Ne$(e,\nu_e)^{20}$F$(e,\nu_e)^{20}$O take place and ignite O-Ne deflagration around the center. In this paper, we perform two-dimensional hydrodynamics simulations of the propagation of the O-Ne flame to see whether such a flame induces a collapse of the O+Ne+Mg core due to subsequent electron capture behind the flame or triggers a thermonuclear explosion. We present a series of models to explore how the outcome depends on model parameters for the central density in the range from $10^{9.80}$ to $10^{10.20}$ g cm^{-3}, flame structure of both centered and off-centered ignition kernels, special and general relativistic effects, turbulent flame speed formula and the treatments of laminar burning phase. We find that the O+Ne+Mg core obtained from stellar evolutionary models has a high tendency to collapse into a neutron star. We obtain the bifurcation between the electron-capture collapse and thermonuclear explosion. We discuss the implication in nucleosynthesis and the possible observational signals of this class of supernovae.

Keywords: hydrodynamics – supernovae: general

1. INTRODUCTION

1.1. *Formation and Evolution of Degenerate ONeMg Cores*

Stars with a mass between 8 and 10 $M_\odot$ have an interesting transition from massive white dwarf (WD) formation (e.g., Sugimoto & Nomoto 1980; Nomoto & Hashimoto 1988; Nomoto et al. 2013) to core collapse supernova (CCSN) (e.g., Arnett 1996). WD with a mass below $M_{\rm up,C} = 7 \pm 2$ $M_\odot$ can form a CO WD (e.g., Nomoto 1982; Karakas 2017). Above that, C-burning in the core produces an oxygen-neon-magnesium (ONeMg) core. The helium shell expands and is dredged up by surface convection (Nomoto 1987). The final ONeMg core mass depends on the competition between the mass deposition from H-burning in the envelope and the mass loss by thermal pulses (e.g., Siess 2007; Pumo et al. 2009; Langer 2012)). In the transition mass, Ne can burn spontaneously in an ONeMg core above 1.37 $M_\odot$ (Nomoto 1984), while a hybrid CO-ONeMg WD can be resulted near this transition mass (Doherty et al. 2015; Woosley & Heger 2015).

Once the ONeMg core reaches a central density of 10^9 g cm^{-3}, odd number isotope pairs (^{25}Mg, ^{25}Na), (^{23}Na, ^{23}Ne), and (^{25}Na, ^{25}Ne), undergo URCA processes (electron captures and β decays, see e.g. Schwab et al. (2017) for the CO WD case) with their rates computed in e.g. Toki et al. (2013); Suzuki et al. (2016). At $10^{9.6}$ g cm^{-3}, electron capture on ^{24}Mg may further create steep electron fraction $Y_{\rm e}$ gradient, which may trigger semi-convection. The lowered $Y_{\rm e}$ makes the core further contract (Miyaji et al. 1980; Nomoto et al. 1982; Nomoto 1987). Meanwhile the electron capture heats the core by its gamma ray deposition. Depending on the treatment of convection, Schwarzschild criterion (Miyaji et al. 1980; Nomoto 1987; Takahashi et al. 2013; Jones et al. 2014) or Leduoux criterion (Miyaji & Nomoto 1987; Hashimoto et al. 1993; Jones et al. 2013; Schwab et al. 2015), they give a range of ignition density from $10^{9.95}$ g cm^{-3} (Ledoux criterion) to $10^{10.2}$ g cm^{-3} (Schwarzschild criterion).

Electron capture supernova (ECSN) is one of the channels for low-mass neutron star (NS) formation, similar to the accretion-induced collapse (Canal & Schatzman 1976). However, the exact details remain a matter of debate due to observational constraints (see

e.g., Mochkovitch & Livio 1989; Yoon et al. 2007; Dessart et al. 2006).

1.2. *Physics of ONe-Deflagratione*

In the high-density (10^9 g cm^{-3}) low-temperature (10^8 K) environment (Nomoto 1984) in the ONeMg core, the weak interactions become important. Beyond $\sim 10^9$ K, O-burning in the core becomes short enough than the hydrodynamics timescale $t_{\rm hyd}$. Nuclear runaway can take place. How the runaway takes place of course depends on the convection timescale $t_{\rm conv}$. When the nuclear reaction timescale $t_{\rm nuc} < t_{\rm hyd} < t_{\rm conv}$, the center is likely for the first runaway to take place, which propagates in the form of deflagration (Timmes & Woosley 1992). The burnt matter has a lower equilibrium $Y_{\rm e}$ owing to a faster electron capture rate at a high density. Therefore the outcome of ECSN is more subtle because the electron capture can suppress the propagation of the nuclear flame, or may even trigger the collapse. To model the turbulent flame properly, multi-dimensional simulations are naturally required.

The nuclear deflagration has been extensively studied and modelled in the Type Ia supernova literature (Reinecke et al. 1999, 2002a,b; Röpke 2005; Röpke & Hillebrandt 2005; Röpke et al. 2007; Ma et al. 2013; Fink et al. 2014; Long et al. 2014). By electron conduction, the deflagration wave propagates in a subsonic velocity and the speed increases with density (Timmes & Woosley 1992). Deflagration is susceptible to fluid advection and hydrodynamical instabilities including the Rayleigh-Taylor instabilities, Kelvin-Helmholtz instabilities and Landau-Derrieius instabilities (Timmes & Woosley 1992; Livne & Arnett 1993; Röpke et al. 2004a,b; Bell et al. 2004a,b). It can have a complex geometry and an explicit front-capturing scheme is often essential for an accurate description to the evolution of the deflagration wave (Osher & Sethian 1988). Due to the sub-sonic nature of the flame, the burnt matter may have sufficient time to expand and relax isobarically (Khokhlov et al. 1997), which creates a density contrast with respect to the fuel. The matter at high density ($> 5 \times 10^9$ K) may release sufficient energy to make the matter reach nuclear statistical equilibrium (NSE). The photo-disintegration of iron-peak elements in the ash and its further electron capture may also alter the structure of the laminar deflagration wave.

1.3. *Motivation*

The uncertainties in the input physics of stellar evolution near the ignition of the ONeMg core give rise to the uncertainties in the initial model. The uncertainties originate from the needs of an extensive nuclear network for the weak interaction process, the treatment of URCA process and its associated convection, and the possibility of (semi-)convection near the core. The ignition density, its position and size are not yet well constrained. Furthermore, the results depend on the nature of turbulent flame (Nomoto & Kondo 1991), which relies on multi-dimensional simulations. The first three-dimensional realization of this phase in Jones et al. (2016) demonstrates the importance of the input physics. Their work shows that the Coulomb correction in the equation of state can result in different explosion strength. The choice of convection criteria, which affects the ignition density, and the numerical resolutions can also alter the final explosion strength. In Jones et al. (2019), the nucleosynthesis based on their previous work is computed with a large nuclear network including 5234 isotopes. Their models can reproduce features of a recently observed Mn-enhanced low mass WD LP 40-365 (Raddi et al. 2018). These results inspire us to examine the role of input physics of ECSN modeling carefully in order to pin down the final fate of ECSN. To do so we use the two-dimensional hydrodynamics code for the computation. The two-dimensional model allows us to explore the parameter space to extract the dependence of input physics in a reasonable computational time.

In Section 2 we briefly outline our hydrodynamics code and the updates employed to model the pre-collapse phase. In Section 3 we report our results of our parameter study. It includes the array of models we used to follow the evolution of ONeMg core. This aims at studying the post-runaway evolution of the ONeMg core at different 1. central density, 2. initial flame structure, 3. initial flame position, 4. flame physics and 5. pre-runaway configuration. In Section 4 we discuss how our results can be understood collectively for future models given by stellar evolution. We also compare our results with some models presented in the literature. Then, we discuss the possible observational constraints on ECSN. At last we present our conclusion. In the appendix we present briefly the possible observational consequences when the ECSN collapses by doing one-dimensional simulations with neutrino transport (the advanced leakage scheme).

2. METHODS

We use the two-dimensional hydrodynamics code developed for supernovae and nucleosynthesis. We refer the readers to Leung et al. (2015a,b); Leung & Nomoto (2017); Nomoto & Leung (2017b); Leung & Nomoto (2018) for a detailed description of the code and its previous applications. We also refer the refer the readers to Nomoto & Leung (2017a) for detailed motivations

of connecting AGB-star to ECSN. The input physics of ECSN is in general similar to Type Ia supernovae since nuclear reactions and electron capture are the principle input physics. In Table 1 we tabulate the governing physics and their typical values for these two types of simulations to demonstrate how much they are similar to each other and what additional physics components are necessary. Here we briefly describe the physics included in the code.

2.1. *Hydrodynamics*

The code solves the Euler equations in cylindrical coordinate. The simulation box use the same grid mesh of 400^2 in the $r-$ and $z-$directions at ~ 4 km. Courant factor is fixed at 0.25. Only a quadrant of sphere is modeled where the inner (outer) boundaries are chosen as reflective (outgoing). We use the fifth-order weighted-essentially non-oscillatory (WENO) scheme for spatial discretization (Barth & Deconinck 1999) and the five-step third-order non-strong stability-preserving Runge-Kutta (NSSP-RK) scheme (Wang & Spiteri 2007) for time-discretization. We use the Helmholtz equation of state (Timmes & Arnett 1999). This equation of state accounts for the contribution of ideal electron gas at arbitrarily degenerate and relativistic levels, ions in the form of a classical ideal gas, photon gas with Planck distribution and the electron-positron annihilation pairs. Level set method is used for tracking the flame geometry.

We use the turbulent flame prescription the same as that in SN Ia, the effective flame speed is proportional to the laminar flame speed $v_{\rm lam}$ and the velocity fluctuation from turbulent v'. (See also Pocheau (1994); Niemeyer et al. (1995); Schmidt et al. (2006); Leung et al. (2015a) for the general formulation of turbulent flame). In this work, we choose

$$v_{\rm turb} = v_{\rm lam}\left[1 + C_t\left(\frac{v'}{v_{\rm lam}}\right)^n\right]^{1/n}. \qquad (1)$$

We choose $n = 2$ following Schmidt et al. (2006), which represents Gaussian velocity distribution and self-similarity in the flame structure. The value C_t is fixed by matching the asymptotic behaviour of turbulent flame from experiments. In Schmidt et al. (2006), C_t is picked as $4/3$. The laminar speed is a function of density and ^{16}O mass fraction as given in Timmes & Woosley (1992). The one-equation model (Niemeyer et al. 1995) is used for modeling the growth and decay of sub-grid turbulence. We define the specific kinetic energy density in the sub-grid scale $q_{\rm turb} = |\vec{v}|'^2/2$. This energy density is a scalar which follows fluid advection and exchanges energy with the internal energy of the fluid. Depending on the context, the source terms of sub-grid turbulence $\dot{q}_{\rm turb}$ can contain different terms. In a star, $\dot{q}_{\rm turb} = \dot{q}_{\rm prod} + \dot{q}_{\rm diss} + \dot{q}_{\rm comp} + \dot{q}_{\rm RT} + \dot{q}_{\rm diff}$. The terms on the right hand side stand for turbulence production by shear stress, turbulence dissipation, turbulence generation by compression, production by Rayleigh-Taylor instabilities and turbulent diffusion.

2.2. *Microphysics*

In this article, we follow the burning scheme prescription proposed in Townsley et al. (2007). This helps to improve the description of chemical composition in the ash, which can be very different from the currently used 7-isotope network (including ^{4}He, ^{12}C, ^{16}O, ^{20}, ^{24}Mg, ^{28}Si and ^{56}Ni). We introduce the quantities $\bar{Y}$, $\bar{q}_B$ and ϕ_i ($i = 1, 2, 3$). They represent the inverse of mean atomic mass ($1/\bar{A}$), binding energy and the burning progress variables. They are also scalars transportable by fluid advection. Operator splitting is used to solve separately the hydrodynamics and nuclear reaction. In the hydrodynamics phase, these quantities are also transported by the fluid, namely

$$\frac{\partial \bar{Y}}{\partial t} + \vec{v}\cdot\nabla\bar{Y} = \dot{\bar{Y}}, \qquad (2)$$

$$\frac{\partial \bar{q}_B}{\partial t} + \vec{v}\cdot\nabla\bar{q}_B = \dot{\bar{q}}_B. \qquad (3)$$

After each step, the mean atomic mass and mean atomic number are reconstructed by $1/\bar{Y}$ and $Y_{\rm e}/\bar{Y}$. These two quantities are passed to the equation of state subroutine to find the derived thermodynamics quantities including the pressure and its derivatives with respect to density and temperature.

After the hydrodynamics substep, we solve the nuclear burning phase. ϕ_1, ϕ_2 and ϕ_3 represent the burning of ^{20}Ne, burning until NQSE and from NQSE to NSE. The level-set method is used for controlling the energy release in ϕ_1. To prevent burnt matter from repeatedly release energy due to numerical diffusion, all ϕ_1, ϕ_2 and ϕ_3 are restricted to be monotonically increasing and ϕ_2 (ϕ_3) is allowed to evolve only when ϕ_1 (ϕ_2) burning has finished. Their evolution also satisfies the following equations

$$\frac{\partial \phi_i}{\partial t} + \vec{v}\cdot\nabla\phi_i = \dot{\phi}_i, \qquad (4)$$

where $i = 1, 2, 3$. We also apply operator splitting for the advection terms and the source terms. The source terms are solved analytically. We remark that for the fluid elements which are not in NSE, no electron capture takes place. This is a good approximation because the electron capture rate below 5×10^9 K is in general much slower than the hydrodynamical timescale.

Table 1. Comparison between the input physics of Type Ia supernova and electron capture supernova.

Input physics	ECSN	Type Ia supernova
Central density	$\sim 10^{10}$ g cm^{-3}	$10^{7} - 10^{10}$ g cm^{-3}
Mass	1.38	0.9 - 1.38
$Y_{\rm e}$ range	0.37 - 0.50	0.44 - 0.50
Composition	ONe-rich matter	CO-rich matter
Peak Temperature	$\sim 10^{10}$ K	$\sim 10^{10}$ K
Energy production	ONe- and Si-burning and NSE	CO-burning, Si-burning and NSE
Electron capture	NSE matter	NSE matter

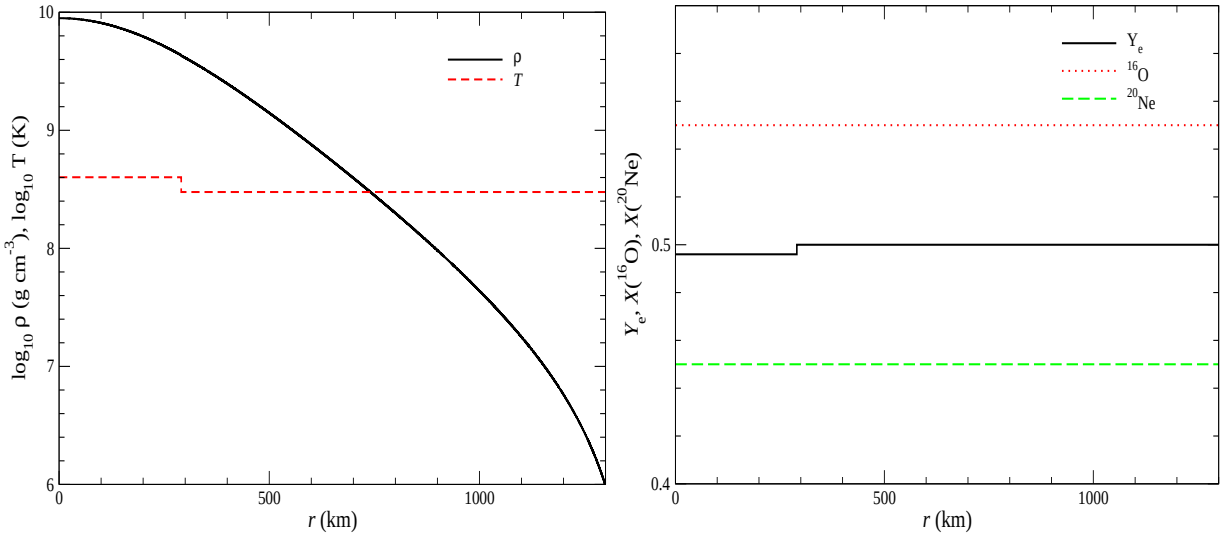

Figure 1. (left panel) The initial profile based on Model c3-09950-N for the density and temperature. (right panel) Similar to the left panel, but for the $Y_{\rm e}$ and abundances for major isotopes.

2.3. *NSE and weak interactions*

To couple the hydrodynamics with an extended nuclear reaction network for accounting for the low $Y_{\rm e}$ matter found in ECSN, we prepare the NSE composition by the 495-isotope network with isotopes from ^{1}H to ^{91}Tc, (Timmes 1999) as a function of density ρ, temperature T and $Y_{\rm e}$. The network also includes the Coulomb correction factor (Kitamura 2000). Matter with a temperature above 5×10^{9} K is assumed to be in the NSE. We require the new composition $X_{\rm new}$, new temperature $T_{\rm new}$ and the new specific internal energy $\epsilon_{\rm new}$ satisfies

$$\frac{\epsilon_{\rm new}-\epsilon}{\Delta t} = N_A(m_n - m_p - m_e)\frac{\Delta Y_{\rm e}}{\Delta t} + \dot{q}_\nu + \frac{q_B(X_{\rm NSE,\ new}) - q_B(X_{\rm NSE})}{\Delta t}. \quad (5)$$

We remark that the NSE composition is a function of density, temperature and $Y_{\rm e}$ that $X_{\rm NSE,\ new} = X_{\rm NSE}(\rho_{\rm new}, T_{\rm new}, Y_{\rm e,new})$. The source terms on the right hand side are the change of the binding energy due to composition change, the energy loss due to neutron-proton mass difference and the energy loss by neutrino emission during electron capture.

To obtain the electron capture rates at low $Y_{\rm e}$, we follow Seitenzahl et al. (2010); Jones et al. (2016) and extend the electron capture rate table by including neutron-rich isotopes. Individual electron capture rates given in Langanke & Martinez-Pinedo (2001) and Nabi & Klapdor-Kleingrothaus (1999) are used. We solve

$$\frac{dY_{\rm e}}{dt} = \sum_i X_i \frac{m_B}{m_i}(\lambda_i^{\rm ec} + \lambda_i^{\rm pc} + \lambda_i^{\rm bd} + \lambda_i^{\rm pd}), \quad (6)$$

where m_B and m_i are the baryon mass and the mass of the isotope i. D/Dt is the derivative in the rest frame of the fluid, $\lambda_{\rm ec}$, $\lambda_{\rm pc}$, $\lambda_{\rm bd}$ and $\lambda_{\rm pd}$ are the rates of electron capture, positron capture, beta-decay and positron-decay of the isotope i respectively in the units of s^{-1}.

3. MODELS AND RESULTS

3.1. *Initial Model*

In this section we describe how we prepare the initial condition for the hydrodynamics run. We use

the ONeMg core structure derived from Schwab et al. (2015). The inner part imitates the zone where electron capture begins to take place. It has thus a lower Y_e and a higher temperature in the inner part and vice versa in the outer part with $(Y_e, T) = (0.496, 4 \times 10^8$ K) for the inner part and $(Y_e, T) = (0.5, 3 \times 10^8$ K) for the outer part. We assume the chemical composition variation is small enough that it remains $X(^{16}\mathrm{O}) = 0.55$ and $X(^{20}\mathrm{Ne}) = 0.45$ throughout the star. In order to maintain a high level of hydrostatic equilibrium, we do not map the initial model directly from stellar evolutionary model, instead we build the initial model by solving the related equation for the given temperature and Y_e profile. In Figure 1 we plot the initial density, temperature, Y_e and abundance profiles for Model c3-09950-N.

3.2. *Numerical Models*

3.2.1. *Uncertainties in Stellar Evolutionary Models*

The uncertainties in the evolution of ONeMg cores lead to the ambiguity of the final evolution of ONeMg cores. One is the semi-convection associated with electron captures. Depending on the efficiency of core convection after O burning has started, the ONe deflagration density in the ONeMg can change from $\sim 10^{9.95}$ (Ledoux criterion) up to $\sim 10^{10.2}$ g cm^{-3} (Schwarzschild criterion). More efficient mixing leads to a higher central density (Takahashi et al. 2013). Therefore, $10^{9.95}$ g cm^{-3} set by the Ledoux-criterion is the lower limit to the deflagration density.

The second uncertainty is the initial flame structure. The development of the initial flame is sensitive to the internal turbulent and convective motion of the star. However, in stellar evolution, which is modelled in one dimension, the non-radial motion of matter is neglected. In particular, local turbulence can provide velocity and temperature fluctuations, which can be important near the runaway phase. An efficient convection may smooth out temperature inversion in the core and enhance centered burning. The initial flame in the ONeMg core, similar to SNe Ia, cannot be constrained if the pre-supernova convective structure is not well modeled.

The third uncertainty is the relativistic effects. The impact of relativistic effects is unclear. In the ONeMg core, the density in the core is sufficiently high that the electrons are ultra-relativistic. The contribution of the pressure and internal energy as a gravity source can be non-negligible. One has to study how these components affect the dynamics, and whether the collapse criteria change with them.

The fourth uncertainty is the coupling of turbulence and flame physics. The turbulent flame formalism assumes the effective flame propagation speed is a function

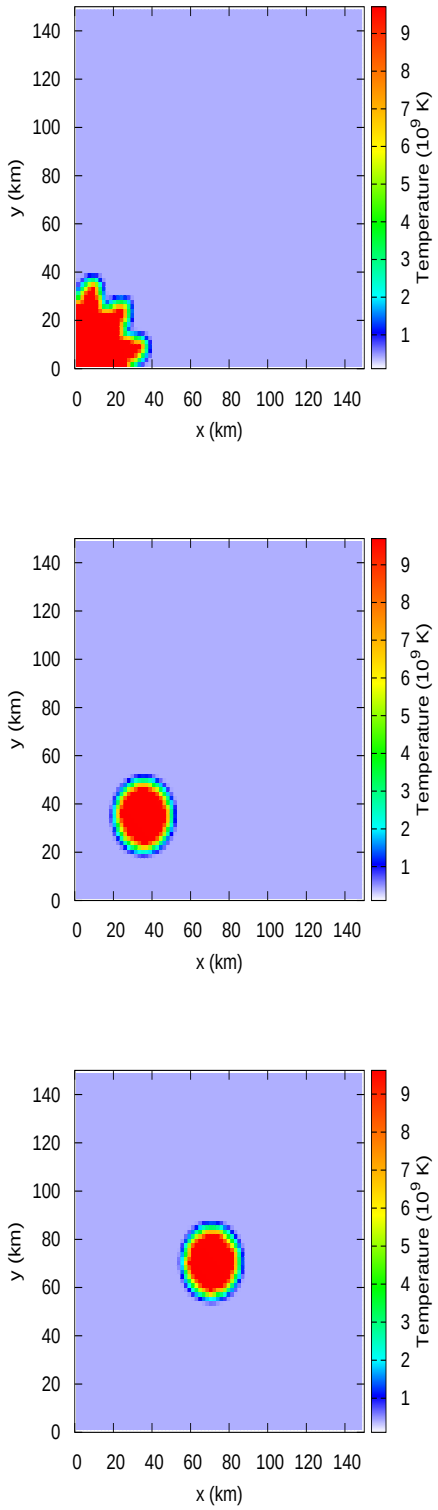

Figure 2. (top panel) The temperature colour plot for the initial flame profile *c*3 using Model c3-09950-N. (middle panel) Similar to the left panel, but for the initial flame profile *b*1*a*. (bottom panel) Similar to the left panel, but for the initial flame profile *b*1*b*.

of velocity fluctuation from eddy motion. However, no experimental data is available for flame to propagate at such high Reynolds number $Re \sim 10^{14}$. There are only similar experiments for the terrestrial flame and theoretical arguments based on self-similarity (see e.g. Pocheau 1994; Hicks 2015). In particular the asymptotic velocity of turbulent flame remains unclear.

3.2.2. *Model Description*

The model parameters spanned in this work attempt to cover the uncertainties left in the stellar evolution modeling. In Table 2, we tabulate the initial setting of our hydrodynamics models. The initial model is built by making reference to the pre-deflagration model as computed in Schwab et al. (2015). In their models, the pre-deflagration ONeMg core consists of three parts, 1. the outer envelope where no burning occurs, 2. the outer core where hydrostatic burning of ^{24}Mg carries out, and 3. the inner core where electron capture and faster nuclear reactions occur. We use their temperature and Y_e profiles to construct our initial model at different central densities. However, we do not resolve the most inner core around 10^{-4} $M_\odot$ which is equivalent to less than a few grid points of our simulations Schwab et al. (2015).

To start the flame, we patch an initial flame of similar size to mimic that deflagration in the central region has already started. However, we remarked that the precise structure of the initial deflagration requires full multi-dimensional simulations right after the first nuclear runaway has started. We therefore implemented different flame structure so as to mimic the different possible outcomes. In particular, we include the $c3$, $b1a$, $b1b$ and $b5$ flame (See Figure 2 or Reinecke et al. (1999) for graphical illustrations). The $c3$ flame is the same "three-finger" structure as in Niemeyer et al. (1995). The "finger shape" can enhance the development of Rayleigh-Taylor instabilities. Also, this shape prevents the development of enhanced flow along the boundary, which might not be physical. A $c3$ flame includes an outer radius of $\sim$ 20 km and an inner radius of 10 km. The flame structure is similar to what we use to start the deflagration phase in Leung et al. (2015a,b) with a smaller size. The $b1a$ flame assumes a ring of radius 15 km located at 50 km away from the center. In Figure 2 we plot the temperature colour plot to show the initial flame structures $c3$, $b1a$ and $b1b$ respectively. We also include variations of the $c3$ flame by magnifying or diminishing its size to achieve different initial burnt masses $M_{\rm burn,ini}$. This attempts to overcome the uncertainties in the unresolved region where the final hydrostatic oxygen burning takes place and triggers the thermonuclear runaway.

3.3. *Effects of Central Density*

3.3.1. *Model with a Centered Ignition Kernel*

In this part we discuss the global behaviour of the ONeMg core which is ignited by a centered flame for different central density.

In all our simulations, we follow the evolution of each model until the central density reaches 10^{11} g cm^{-3} (collapse case) or when the total time reaches 1.5 s (expansion case). For models with heading of $c3$ (Models c3-09800-N, c3-09850-N, c3-09900-N, c3-09925-N, c3-09950-N, c3-09975-N, c3-10000-N), we compute the deflagration phase of the ONeMg core at different central densities but with the same flame structure of $c3$ using the Newtonian gravity. (We postpone the comparison of flame development in Section 3.6.1). In this series of model, when central density increases, the total mass increases from 1.38 to 1.39 $M_\odot$. Only a mild rise in mass is observed due to the highly degenerate electron gas. On the other hand, the radius decreases from 1.54×10^3 to 1.36×10^3 km. The opposite variations in the mass and radius are consistent with the ONeMg core model. The minimum Y_e also drops when ρ_c increases, because the electron capture at high Y_e increases as density increases. The collapse time, which is related to the drop of Y_e also drops. Similarly, we observe a drop in the burnt mass.

For models which expand, Models c3-09800-N and c3-09850-N, about 1 $M_\odot$ is burnt. For the collapsing models, the faster they collapse, a smaller amount of fuel is burnt. The final energy is much lower than typical Type Ia supernovae, which is $\sim 10^{49}$ erg, in contrast to the higher nuclear energy release, which is $\sim 10^{50}$ erg.

In the upper panel of Figure 3 we plot the central densities for Models c3-09800-N, c3-09850-N, c3-09900-N, c3-09925-N, c3-09950-N, c3-09975-N, c3-10000-N. In all models, the central densities increase for the first 0.5 - 0.7 s where the electron capture dominates the dynamics. Models with a central density greater than $10^{9.9}$ g cm^{-3} collapse directly within 0.5 - 1.0 s, where the contraction rate increases with the central density. Models with lower initial central densities expand after $\sim$ 0.6 s, showing that the energy released by deflagration is sufficient to balance the loss of pressure during the electron captures.

In the lower panel of Figure 3 we plot the central electron fraction as a function of time for the seven models as the upper panel. Unlike the central densities, the central electron fraction drops drastically for about 0.5 s until the decreasing rate slows down to some intermediate values. The equilibrium Y_e decreases while the initial central density increases. For the models which directly collapse, the drop of central Y_e slows down at $Y_e \approx 0.38$ around 0.3 to 0.5 s. Then, it further decreases to 0.36,

Table 2. The initial configurations and the final results of the simulations. $\log_{10}\ \rho_c$ is the logarithmic of initial central density in units of g cm^{-1}. $Y_{e,\ \mathrm{in}}$ and $Y_{e,\ \mathrm{out}}$ are the initial electron fraction of the core and envelope. $Y_{e,\mathrm{min}}$ is the minimum electron fraction reached in the simulation. t_{coll} is the time lapse from the beginning of simulation to the moment where the central density exceeds 10^{11} g cm^{-1}. No t_{coll} is given for models which do not collapse. M and M_{burn} are the initial mass and the amount of matter burnt by deflagration in units of $M_\odot$. R is the initial radius of the star in 10^3 km. E_{tot} and E_{nuc} are the final energy and the energy released by nuclear reactions in the units of 10^{50} erg. E_{tot} is not recorded for models which do not explode. Results stands for the final fate of the ONeMg core, where "C" and "E" stand for the core in the state of collapse and expansion at the point when the simulation is stopped. Gravity means the use of Newtonian gravity source or the pseudo-relativistic gravity source.

Model	$\log_{10}\rho_c$	flame	$Y_{e,\ \mathrm{in}}$	$Y_{e,\ \mathrm{out}}$	M	R	$Y_{e,\mathrm{min}}$	t_{coll}	M_{burn}	E_{tot}	E_{nuc}	Gravity	Results
c3-09800-N	9.80	*c*3	0.496	0.5	1.38	1.54	0.397	N/A	1.12	-0.16	8.19	N	E
c3-09850-N	9.85	*c*3	0.496	0.5	1.38	1.49	0.387	N/A	1.21	0.23	9.67	N	E
c3-09900-N	9.90	*c*3	0.496	0.5	1.39	1.45	0.357	0.96	1.00	N/A	7.92	N	C
c3-09900-R	9.90	*c*3	0.496	0.5	1.39	1.45	0.357	0.96	1.00	N/A	8.68	R	C
c3-09925-N	9.925	*c*3	0.496	0.5	1.39	1.42	0.354	0.76	0.52	N/A	6.83	N	C
c3-09950-N	9.95	*c*3	0.496	0.5	1.39	1.40	0.353	0.69	0.40	N/A	6.83	N	C
c3-09975-N	9.975	*c*3	0.496	0.5	1.39	1.38	0.353	0.63	0.34	N/A	6.70	N	C
c3-10000-N	10.0	*c*3	0.496	0.5	1.39	1.36	0.353	0.59	0.30	N/A	6.56	N	C
c3-10000-R	10.0	*c*3	0.496	0.5	1.39	1.36	0.353	0.59	0.30	N/A	6.56	R	C
c3-10200-N	10.2	*c*3	0.496	0.5	1.39	1.19	0.351	0.37	0.18	N/A	4.78	N	C
c3-10200-R	10.2	*c*3	0.496	0.5	1.39	1.19	0.351	0.37	0.18	N/A	4.78	R	C
b1a-09875-N	9.875	*b*1*a*	0.496	0.5	1.38	1.47	0.395	N/A	1.20	0.25	10.18	N	E
b1a-09900-N	9.90	*b*1*a*	0.496	0.5	1.39	1.45	0.382	N/A	1.32	0.26	12.39	N	E
b1a-09900-R	9.90	*b*1*a*	0.496	0.5	1.39	1.45	0.358	N/A	1.28	0.39	11.94	R	E
b1a-09925-N	9.925	*b*1*a*	0.496	0.5	1.39	1.42	0.364	0.73	0.68	N/A	6.21	N	C
b1a-09950-N	9.95	*b*1*a*	0.496	0.5	1.39	1.40	0.363	0.62	0.48	N/A	5.47	N	C
b1a-10000-N	10.0	*b*1*a*	0.496	0.5	1.39	1.36	0.360	0.51	0.34	N/A	4.37	N	C
b1b-09900-N	9.90	*b*1*b*	0.496	0.5	1.39	1.45	0.395	N/A	1.17	0.13	9.91	N	E
b1b-09950-N	9.95	*b*1*b*	0.496	0.5	1.39	1.40	0.388	N/A	1.37	0.27	13.47	N	E
b1b-09975-N	9.975	*b*1*b*	0.496	0.5	1.39	1.38	0.364	0.58	0.74	N/A	6.98	N	C
b1b-10000-N	10.0	*b*1*b*	0.496	0.5	1.39	1.36	0.357	0.49	0.54	N/A	5.94	N	C
mc3-09850-N	9.85	*mc*3	0.496	0.5	1.38	1.49	0.395	N/A	1.10	0.23	9.17	N	E
mc3-09900-N	9.90	*mc*3	0.496	0.5	1.39	1.45	0.375	N/A	1.36	-0.37	10.07	N	E
mc3-09925-N	9.925	*mc*3	0.496	0.5	1.39	1.42	0.355	0.64	0.53	N/A	5.86	N	C
mc3-09950-N	9.95	*mc*3	0.496	0.5	1.39	1.40	0.355	0.56	0.40	N/A	5.06	N	C
bc3-09925-N	9.925	*bc*3	0.496	0.5	1.39	1.42	0.395	N/A	1.14	0.13	10.12	N	E
bc3-09950-N	9.95	*bc*3	0.496	0.5	1.39	1.40	0.386	N/A	1.26	0.48	12.12	N	E
bc3-09975-N	9.975	*bc*3	0.496	0.5	1.39	1.38	0.354	0.54	0.73	N/A	6.94	N	C
b1b-09950-N-Lam	9.95	*b*1*b*	0.496	0.5	1.39	1.40	0.375	1.15	0.02	N/A	0.07	N	C
b1b-09975-N-Lam	9.975	*b*1*b*	0.496	0.5	1.39	1.38	0.377	1.34	0.04	N/A	0.88	N	C
b1b-10000-N-Lam	10.0	*b*1*b*	0.496	0.5	1.39	1.36	0.374	0.97	0.02	N/A	0.16	N	C
bc3-09950-N-vf025	9.95	*bc*3	0.496	0.5	1.39	1.40	0.368	0.55	0.07	N/A	2.42	N	C
bc3-09950-N-vf050	9.95	*bc*3	0.496	0.5	1.39	1.40	0.368	0.56	0.71	N/A	5.74	N	C
bc3-09950-N	9.95	*bc*3	0.496	0.5	1.39	1.40	0.386	N/A	1.26	0.48	12.12	N	E
bc3-09950-N-B025	9.95	*bc*3	0.496	0.5	1.39	1.40	0.365	0.61	0.51	N/A	4.83	N	C
bc3-09950-N-B050	9.95	*bc*3	0.496	0.5	1.39	1.40	0.367	0.55	0.53	N/A	5.14	N	C
bc3-09950-N-B075	9.95	*bc*3	0.496	0.5	1.39	1.40	0.367	0.54	0.70	N/A	6.28	N	C
bc3-09950-N	9.95	*bc*3	0.496	0.5	1.39	1.40	0.386	N/A	1.26	0.48	12.12	N	E

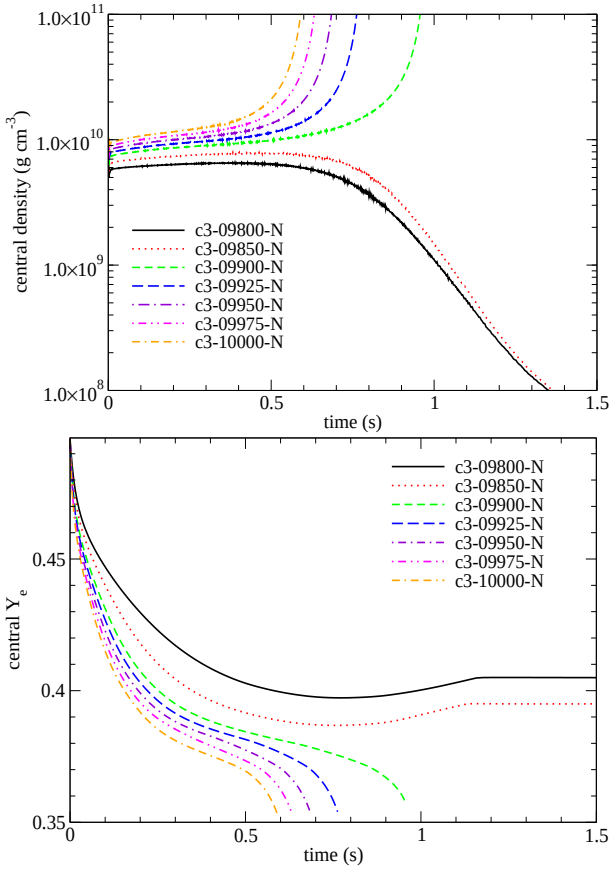

Figure 3. (upper panel) The time evolution of the central density of Models c3-09800-N, c3-09850-N, c3-09900-N, c3-09925-N, c3-09950-N, c3-09975-N and c3-10000-N. Refer to Table 2 for the details of the configurations. All models have the same initial centered flame but at different central densities. (lower panel) The evolution of central Y_e for the same set of models to the upper panel, which compares the effects of initial central density (also initial mass) to the final evolution.

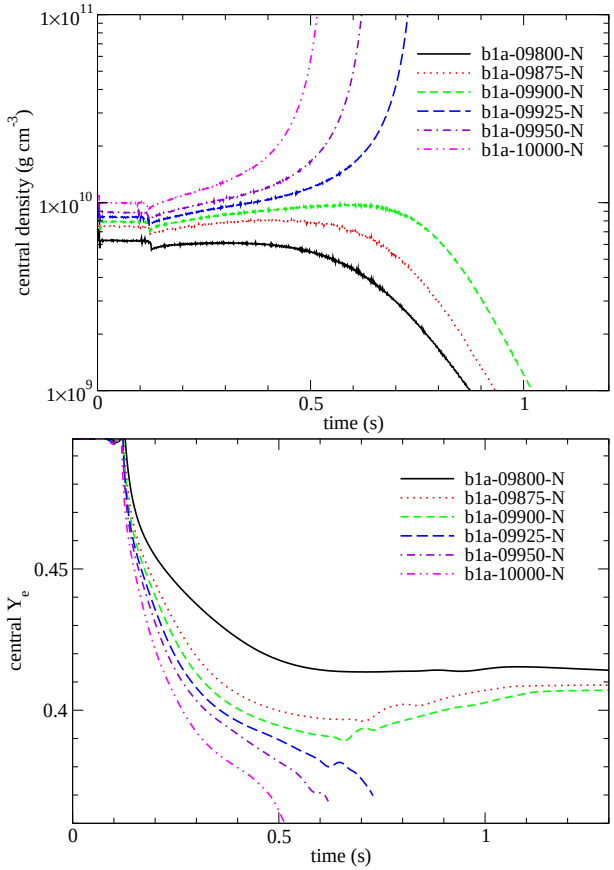

Figure 4. (upper panel) The time evolution of the central density of Models b1a-09875-N, b1a-09900-N, b1a-09925-N, b1a-09950-N and b1a-10000-N. to Figure 3 the models share the same setting except different central densities. (lower panel) The central Y_e for the evolution of the same set of models in the upper panel.

as the central densities of these models further increase to 10^{11} g cm^{-3}. For models which expand, the central electron fraction drops as similar to the collapsing models, but they reach a higher intermediate Y_e compared to those models. In particular, Models c3-09800-N and c3-09850-N show an equilibrium Y_e of 0.39 and 0.40 respectively at $t \approx 0.7 - 0.8$ s after the deflagration has started. Following the expansion of the star, the central Y_e gradually increases and reaches the equilibrium value of ~ 0.40 at $t \approx 1.1$ s.

3.3.2. *The b1a Series*

For models with a heading $b1a$ (Models b1a-09800-N, b1a-09875-N, b1a-09900-N, b1a-09925-N, b1a-09950-N and b1a-10000-N), they are the ONeMg core models similar to above, but with an initial flame $b1a$, which means a flame bubble (a ring in the three-dimension visualization) of a radius 15 km at 50 km away from the ONeMg core center. The initial configurations are prepared from a ONeMg core at hydrostatic equilibrium. The initial masses and radii are the same as those of the $c3$ series. Models b1a-09800-N, b1a-09875-N, b1a-09900-N are exploding while the others are collapsing. In general, the trends of the Y_e at the end of simulations are similar that a higher ρ_c implies a lower Y_e. However, for models with the same central density, Y_e is higher for the $b1a$ flame than the $c3$ flame. Also, less mass is burnt and the direct collapse occurs faster, for the same central density, with an exception of Model b1a-09875-N. Due to a shorter time for the deflagration wave to sweep the fuel before the core collapse, less energy is released by nuclear reactions as the initial central density increases. It can be seen that the general pattern for the $b1a$ series is comparable with the $c3$ series.

In the upper panel of Figure 4 we plot the central density against time similar to Figure 3. Due to the off-

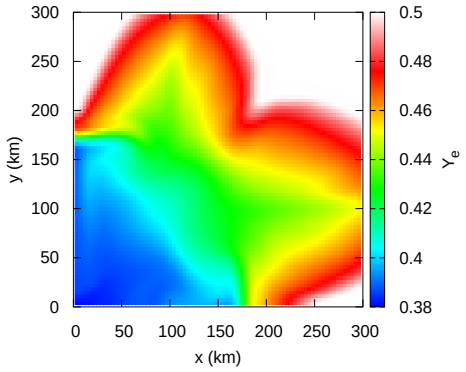

Figure 5. The Y_e distribution of Model b1a-09925-N at $t = 0.625$ s. The aspherical distribution distribution of Y_e can produce bumps in the evolution of Y_e.

center burning, there is no change in the central density before 0.1 s. Once the flame reaches the center, the central density drops rapidly due to the expansion of matter. After the initial expansion, the central densities of all six models increase. Models with an initial central density greater than $10^{9.925}$ g cm^{-3} reach the threshold density at 0.4 - 0.7 s. Again, the collapse time decreases when central density increases. On the contrary, Models b1a-09800-N, b1a-09875-N and b1a-09900-N expand at about 0.5 - 0.7 s. In particular, the central density of Model b1a-09900-N can reach as high as 10^{10} g cm^{-3}, before the expansion takes place. Such high central density can be observed for models near the bifurcation transition, where the flame takes more time in order to grow and balance the electron capture effects.

In the lower panel of Figure 4 we plot similar to 4 but for the central Y_e. Similar to the central density, there is no change in central Y_e before 0.1 second, when the flame has not reached the core. After that, it quickly drops with a rate proportional to the central density, and slows down after it reaches $\sim$ 0.38 - 0.41. For models which directly collapse, the central Y_e quickly resumes its fall again and reaches 0.35 - 0.36 at the end of the simulations. In Models b1a-09925-N and b1a-09950-N, there are mild bumps in central Y_e at $t \approx 0.6$ s. This is because the off-center burning has led to an uneven distribution of Y_e. Unlike the Models with $c3$ flame, the central ignition allows that the matter with the higher densities to be burnt for a longer time, thus having more time for electron capture and a lower Y_e. This creates a distribution of increasing Y_e as moving away from the core. For the $b1a$ cases, the region which undergoes the longest duration of electron capture is away from center. Furthermore, in the core, before the homologous expansion fully develops, mixing from neighbouring cells may also affect the Y_e distribution. The temporary inward flow to the center can also increase the central Y_e. In Figure 5 we plot the Y_e distribution of the Model b1a-09925-N at $t = 0.625$ s. We can see near the center Y_e is not completely spherically symmetric. Such asymmetric may give rise to small scale bumps in the Y_e evolution. However, for Model b1a-10000-N, the direct collapse occurs without reaching any intermediate Y_e. Therefore, the electron capture around all the region is similar. Y_e only drops monotonically with time.

3.3.3. *The b1b Series*

In this series we further study the density dependence of ONeMg core with an off-center flame at 100 km from the origin. The models include Models b1b-09900-N, b1b-09950-N, b1b-09975-N and b1b-10000-N. The flame structure in this series of models is similar to $b1a$, but the "flame ring" is located at 100 km apart from the core. Similar to the $b1a$ series, the initial profiles are exactly the same as the $c3$ series that they share the same mass and radius for the same central density. In this series, Models b1b-09900-N and b1b-09950-N are expanding while the others are directly collapsing. Similar to the two series above, the higher the central density the core has, the lower the final Y_e at the end of simulation and a faster collapse it has. Also, less nuclear energy is released owing to a smaller mass of fuel burnt by deflagration wave.

In the upper panel of Figure 6 we plot the central density against time for the four models similar to Figures 3 and 4. With a flame bubble located farther from center, the flame needs $\sim$ 0.3 s to reach the center, which creates a small drop in the central density. At around 0.5 s, Models b1b-09975-N and b1b-10000-N starts its collapse. The central density of Model b1b-09950 also increases above 10^{10} g cm^{-3} at $\sim$ 0.5 s, but drops again when the star expands at 0.7 s. Model b1b-09900 shows almost no contraction when the electron captures take place at the core. This is because the density is sufficiently low and the initial flame is sufficiently far such that it burns the matter and lets the matter expand before the flame can reach the center.

In the lower panel of Figure 6 we plot the time evolution of central Y_e for the same series of models as in the upper panel. There is no change in Y_e at the first 0.3 s. This is because the flame has not arrived at the core. So, the cold matter cannot carry out efficient electron capture compared to the burnt ash. After the deflagration wave has arrived the center, Y_e drops immediately. The higher the initial central density the model has, the faster the rate of decrease. In Models b1b-09750-N and b1b-10000-N, the electron captures mildly slow down

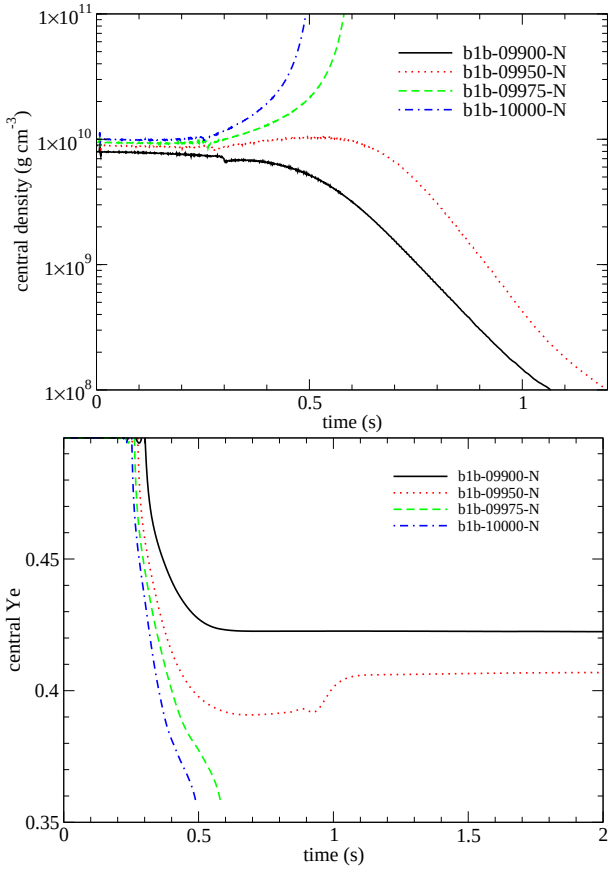

Figure 6. (upper panel) The time evolution of the central density of Models b1b-09900-N, b1b-09950-N, b1b-09975-N and b1b-10000-N.(lower panel) Same as the upper panel, but for the evolution of the central $Y_{\rm e}$ for the same set of models.

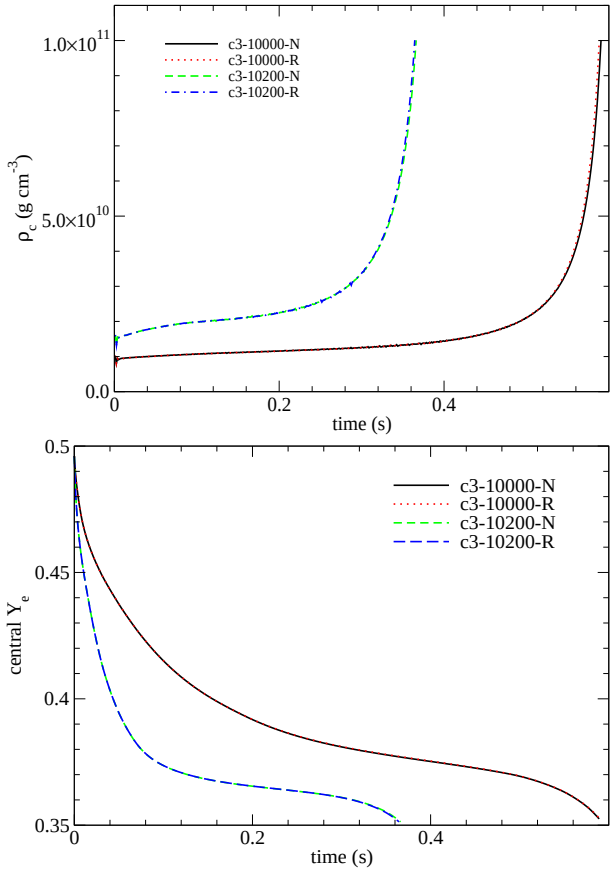

Figure 7. (upper panel) The central density against time for two models with or without relativistic corrections. Model A: $\rho_{c\ (\rm ini)} = 10^{10.0}$ g cm^{-3}. Model B: $\rho_{c\ (\rm ini)} = 10^{10.2}$ g cm^{-3}. Both models have an initial $M_{\rm burn} = 8.56 \times 10^{-4} M_\odot$. (lower panel) Similar to the upper panel, but for the central $Y_{\rm e}$ for the same set of models.

when $Y_{\rm e} = 0.37$, and then the drop resumes again until the end of simulations, down to a value of ≈ 0.36. In contrast, $Y_{\rm e}$ shows an obvious intermediate value at 0.39 and 0.42 for Models b1b-09900-N and b1b-09950-N. The latter one remains the same value after the expansion starts, while the former one slight increases to 0.41, as the matter in the core begins to mix with the surrounding material, which has a higher $Y_{\rm e}$.

We also notice that at early time there is a mild drop of the central density before the flame arriving the center. It is not because the model is not in good equilibrium during construction, but because the initial off-center flame and its subsequent electron capture disturbs the pressure gradient. The core slowly expands to adjust to the presence of the flame.

3.4. *Effects of General Relativity*

Here we study if the relativistic effects can alter the bifurcation criteria of the ONeMg core. In the simulations, we study the counterpart models for Models c3-10000-N and c3-10200-R, namely c3-10000-N, c3-10200-R. These models are the most compact ONeMg cores used in this work, we therefore expect the relativistic effects are the most pronounced. In general to embed the physics of relativistic gravity requires a complete restructure of the code due to the necessary inclusion of the metric tensor. We seek out extension of the Newtonian gravity as a first step. We follow the prescription in Kim et al. (2012). Based on the Poisson equation for the gravitational potential $\nabla^2\Phi = 4\pi G\rho$, where Φ and ρ are the gravitational potential and matter mass density. We replace ρ by $\rho_{\rm active}$, where

$$\rho_{\rm active} = \rho h \frac{1+v^2}{1-v^2} + 2P, \tag{7}$$

and P, v^2 are the fluid pressure and the magnitude square of the velocity. $h = 1 + \epsilon + P/\rho$ is the specific enthalpy of the matter. In this sense, the extra mass-energy owing to the internal energy and the kinematic of the matter is included.

To demonstrate the effects the relativistic correction in the gravitational potential, in the upper panel of Figure 7 we plot the central density for the models with central flame of burnt mass 8.56×10^{-4} $M_\odot$ and with initial central densities $10^{10.0}$ and $10^{10.2}$ g cm^{-3} respectively. In the lower panel of Figure 7 we plot similar to the upper panel but for the central electron fraction. In both cases a direct collapse is observed. The evolution of the central density is not sensitive to the general relativistic corrections in gravity. Models c3-10000-N and c3-10000-R overlap with each other in the figure throughout the simulation, and so are Models c3-10200-N and c3-10200-R. Similar results can be found for the electron fraction.

By combining these models, we showed that when GR correction terms in gravity are included, no observable change in the evolution even for the highest density model $\rho_c = 10^{10.2}$ g cm^{-3}. This suggests that Newtonian gravity is sufficient in following the runaway phase of ONeMg core accurately prior to its onset of collapse.

3.5. *Effects of Initial Flame Size*

The exact size of nuclear runaway is not well constrained because it depends on the competition between the convection efficiency and hydrostatic O-burning in the late phase. Numerically it is difficult to implement due to the sharp Y_e contrast and complication from URCA processes. In general, efficient semi-convection leads to a faster transport of heat produced during electron capture. This smooths the temperature profile and allows a larger initial flame, and raises the ignition density accordingly.

Without knowing the exact details of the initial flame evolution, we try to span the parameter space by considering different flame size for the centered burning model. They include *c*3, *mc*3 and *bc*3. The latter two flame structures are the same as the standard *c*3 flame, but with its size 2 times and 4 times larger. The width of the reaction front is kept to be the same. The case *bc*3 is so extended that it might be non-realizable from typical stellar evolution. We use it for a qualitative comparison in this work.

In the upper panel of Figure 8 we plot the evolution of central density against time for models of different initial flame masses. The initial mass being burnt $M_{\rm burn,ini}$ in NSE ranges from 10^{-4} to 10^{-2} $M_\odot$. For Model c3-09950-N with $M_{\rm burn,ini} \sim 10^{-4}$ $M_\odot$, the central density increases for the first 0.1 s. The models deviate at $\sim$ 0.3 s. Beyond $t = 0.7$ s, the ONeMg core collapses. On the other hand, when $M_{\rm burn,ini} \sim 10^{-3}$ $M_\odot$, a similar evolution occurs but the collapse starts earlier, at 0.5 s after the simulation. When $M_{\rm burn,\ ini} \sim 10^{-2}$ $M_\odot$,

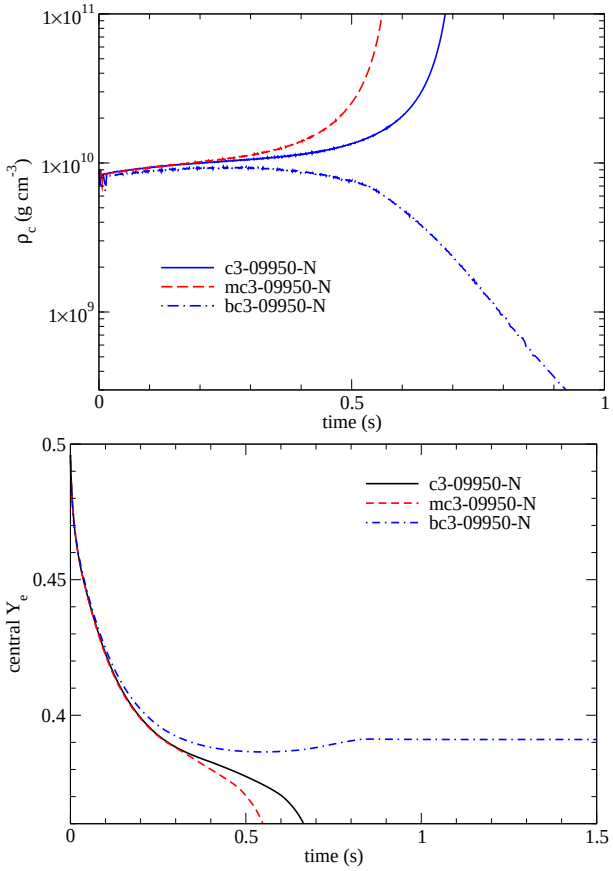

Figure 8. (upper panel) The time evolution of the central density of Models c3-09950-N, mc3-09950-N and bc3-09950-N. (lower panel) Similar to the upper panel but for the central Y_e for the same set of models.

a similar contraction occurs at the beginning, but after $t = 0.5$ s, the star central density decreases, showing that the ONeMg core fails to collapse. Instead, it explodes weakly similar to a Type 1.5x supernova (when the realistic progenitor model including the H-envelope is considered).

In the lower panel of Figure 8 we plot similar to Figure 8 but for the central Y_e. Similar to previous models, all three models show a rapid drop of Y_e once the core is burnt to NSE. It drops to about 0.39 within 0.3 s, and the capture rate slows down. The equilibrium Y_e of c3-09950-N is slightly higher than Models mc3-09950-N and bc3-09950-N. Then at $t = 0.5$ and 0.6 s, Y_e drops rapidly again for the two collapsing models, Models c3-09950-N and mc3-09950-N. However, in Model c3-09950-N, due to expansion, mixing occurs in the core with the matter of the outer zones, which has on average a higher Y_e. Its Y_e slowly increases to 0.39 and remains unchanged after $t = 0.8$ s.

These figures show that the initial flame size also plays a role in determining the collapse condition. In particu-

lar, a small flame $\sim 10^{-4}-10^{-3}\ M_\odot$ favours the collapse scenario, while a large flame favours the expansion scenario.

3.6. *Effects of Flame Physics*

In modeling turbulent flame, a formula describing the relation between the turbulent velocity v' and the effective flame propagation speed $v_{\rm turb}$ is necessary. However, only a statistical description is available due to the stochastic nature of turbulent motion. Also, the terrestrial experiment is not yet capable in reproducing such extreme environment. How the turbulent motion can enhance the propagation of flame and also the effective flame speed remains unclear. In the literature of Type Ia supernova using the turbulent flame model, the typical formula assumes self-similar flame. With the renormalization scheme (Pocheau 1994), the general formula writes

$$v_{\rm turb} = v_{\rm lam}\left[1 + C_n\left(\frac{v'}{v_{\rm lam}}\right)^n\right]^{1/n}, \qquad (8)$$

with $v_{\rm lam}$ being the laminar flame propagation speed while C_n and n are the constant derived from experiments and n describes the velocity spectra of the turbulence structure. This formula has two asymptotic properties which are expected experimentally. 1. The effective propagation speed reduces to the laminar flame speed, when $v' \to 0$. This corresponds to the case that when there is no perturbation to the surface structure of the flame, the flame propagates as a laminar wave. 2. The effective propagation speed has a limit $\approx \sqrt[n]{C_n}v'$. This means that when the fluid motion is highly turbulent, the flame no longer depends on laminar flame speed, but follows only the velocity fluctuation inside the fluid.

However, one shortcoming in this model is that in deriving this formula, an isotropic turbulence is assumed by the renormalization procedure. Gravity makes the radial direction distinctive from the angular directions. Furthermore, the Rayleigh-Taylor instabilities enhances the flame propagation along the radial direction.

Numerically, one has different C_n and n based on the context. In Peter (1999); Schmidt et al. (2006), $C_n = 4/3$ and $n = 2$ which corresponds to the Gaussian distribution of velocity fluctuations. In Hicks (2015), it is shown numerically that for a premixed flame with a one-way reaction such as H_2-air mixture, the relation has a best fit of $C_n = 0.614$ when $n = 2$, while $v_{\rm turb} = v_{\rm lam}(1 + 0.4321\tilde{v}'^{1.997})$ is the best fit with $\tilde{v}'$ being the scaled v'. The variations of this formula demonstrate that the scaling factor C_n and the scaling power n remain poorly constrained.

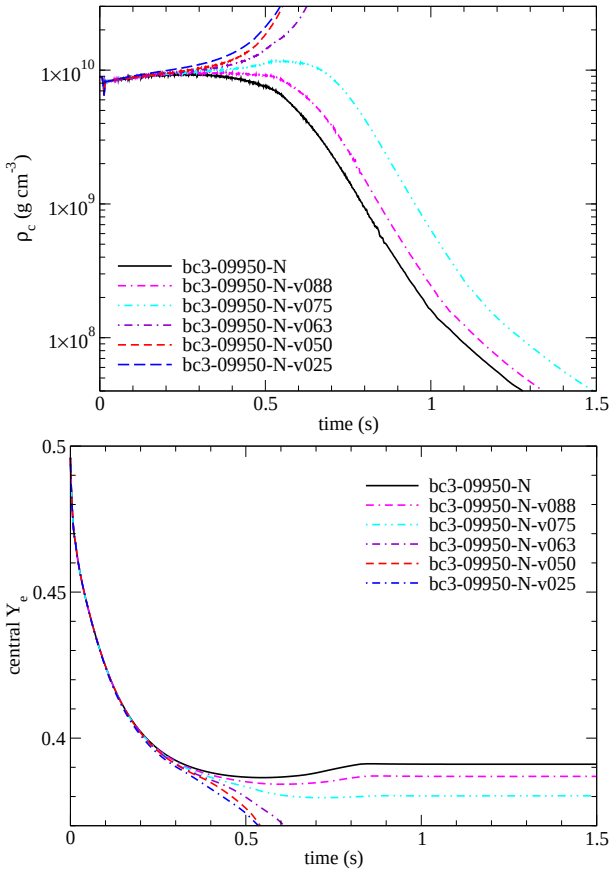

Figure 9. upper panel) The evolution of central density against time for Model bc3-09950-N, bc3-09950-N-vf050 and bc3-09950-N-vf025. Extra models are plotted including Models bc3-09950-N-vf063, bc3-09950-N-vf075 and bc3-09950-N-vf088. (lower panel) Similar to the upper panel but for the central $Y_{\rm e}$ for the same set of models. For the expanding models (Models bc3-09950-N, bc3-09950-N-vf088 and bc3-09950-N-vf075), the flame speed affects final $Y_{\rm e}$.

To understand the effects of this quantity to the ONeMg core evolution, we vary the original value of C_n(denoted as C_{n0}) by considering $C_n = 0.25\ C_{n0}$ and $0.50\ C_{n0}$. They correspond to the turbulent flame where turbulent production is less effective in disturbing the flame structure.

In the upper panel of Figure 9 we plot the central density against time for Models bc3-09950-N, bc3-09950-vf050 and c3-09950-vf025. In this series of models, Models bc3-09950-N explodes while bc3-09950-vf050 and bc3-09950-vf025 collapse. We also plot results from extra models (not included in Table 2) for demonstrating the sensitivity of model results on flame speed by including Models bc3-09950-N-vf063, bc3-09950-N-vf075 and bc3-09950-N-vf088, which are 63 %, 75 % and 88 % of the default flame speed. We choose the bc3 flame instead of the smaller c3, which is less extreme, because

we want to demonstrate that this effect can be important for models near the transition. In particular, in our models, the transition density for the c3 flame is $\sim 10^{9.90}$ g cm^{-3}, using a slower flame does not change the fate of the model at $10^{9.95}$ g cm^{-3} from its fate to collapse into a NS. Thus, we consider the bc3 flame, which expands at a central density of $10^{9.95}$ g cm^{-3}.

The central densities of all three models mildly increase for the first 0.3 s. For the collapsing models, the increase of ρ_c resumes at $t \approx 0.4$ s. On the other hand, for expanding models, ρ_c like in Model bc3-09950-N slowly drops till $t = 0.6$ s. Accompanying with the expansion, its central density rapidly drops after $t = 0.6$ s. At $t = 1$ s, the central density drops to about 1 % of its original value. When the flame speed is faster, the faster the conversion from contraction to expansion and also its rate of drop in the central density.

In the lower panel of Figure 9 we plot the central Y_e similar to Figure 9. In the exploding Model bc3-09950-N, the central Y_e again quickly drops from 0.5 to 0.38 within 0.3 s. Unlike the previous test on the effects of flame size, the large initial flame we used is less changed by the surrounding. Beyond $t = 0.3$ s, the drop of Y_e accelerates again and the central Y_e drops below 0.37 at $t = 0.5$ s. On the other hand, for the models which expand, during its expansion, has its central Y_e slightly relaxed towards 0.38 - 0.39 as its asymptotic value beyond $t = 0.8$ s. We remark that the asymptotic Y_e increases when the flame speed is faster. Notice that the final Y_e determines the characteristic abundance of the ash, especially when they are ejected. The low-Ye ejecta contain a significant overproduction of neutron-rich isotopes, e.g. ^{50}Ti, ^{54}Cr, ^{60}Fe and ^{64}Ni with respect to ^{56}Fe. Such overproduction can be strongly constrained by the galactic chemical evolution. We will discuss further the ejecta properties in Section 4.2.

Combining these three plots, it can be seen that the effective formula of the turbulent flame prescription also plays a role in the ONeMg collapse condition similar to the initial flame size and the properties of the flame kernel. In particular, models tend to collapse (expand) when the flame is slow (fast). This is because the slower flame provides more time for electron capture, thus allowing the star to contract faster than the propagation of flame. Also, the faster flame allows a faster growth of its surface area, which can also balance the effects of decreasing Y_e. However, we also remark that such flip of a model from an expanding model to a collapsing model can be seen only for that near the transition point.

3.6.1. *Extension: Effects of Laminar Flame Propagation*

We remark that the treatment of nuclear flame in the literature does not always assume sub-grid turbulence model (See e.g. Plewa 2007). The flame is only distorted by the smallest resolvable length scale and it is assumed fluid motion below resolvable scale is laminar (Except the perturbation by Rayleigh-Taylor instabilities). This forms another limit in flame propagation.

To demonstrate this limit, we pick a ONeMg configuration where the flame size is the most extensive and explode. Also, our models with very slow flame has unphysical enhancement of flame propagation along the symmetry axis. So, an off-center flame is preferred. We choose the Models b1b-09950-N-Lam, b1b-09975-N-Lam and b1b-10000-N-Lam. (An ending "-Lam" corresponds to the flame which only propagates without sub-grid acceleration.) For the effects of slower flame in general we discuss in Section 4.1.

Models b1b-09950-N-Lam, b1b-09975-N-Lam and b1b-10000-N-Lam collapse into neutron star. In contrast, we compare Model b1b-09950-N-Lam with Model b1b-09950-N, which has the same configuration but with turbulent flame prescription, this model directly expands like a Type 1.5 supernova. On the other hand, when laminar flame prescription is used, the star directly collapses. This shows that the nature of the flame is important for determining the final result of the ECSN. In particular, whether the flame interacts with sub-grid eddy motion, or only interacts with buoyancy smearing, changes the collapse-explode bifurcation of the benchmark model $\rho_c = 10^{9.95}$ g cm^{-3}.

To characterize the difference of flame propagation by the turbulent flame and laminar flame, we plot in Figure 10 the temperature colour plot of Model b1b-09950-N from 0 to 1.25 s at an interval of 0.25 s. The hot elements also trace the flame structure. Here the $b1$ structure is used. The turbulent flame allows the structure to grow rapidly. Within the first 0.5 s, there is a two-bump structure developed and the size has grown to ~ 450 km. At $t = 0.75$ s onwards, the large-scale structure freezes and the two-"finger" shape emerges. At $t = 1.0$ s, the flame expands rapidly to 2000 km, where the surface shows more features when the hydrodynamics instabilities become pronounced.

In Figure 11 we plot similar to Figure 10 but for Model b1b-09950-N-Lam from 0.2 - 1.2 at selected time. A qualitative comparison of the flame structure already demonstrates drastic differences between the propagation of laminar flame and turbulent flame. At early time before 0.4 s, the fluid motion has largely reshaped the original spherical flame. Many small-scale "mushroom shapes" swarm out as a manifestation of the Rayleigh-Taylor instabilities. At $t = 0.6$ s, the flame has finally

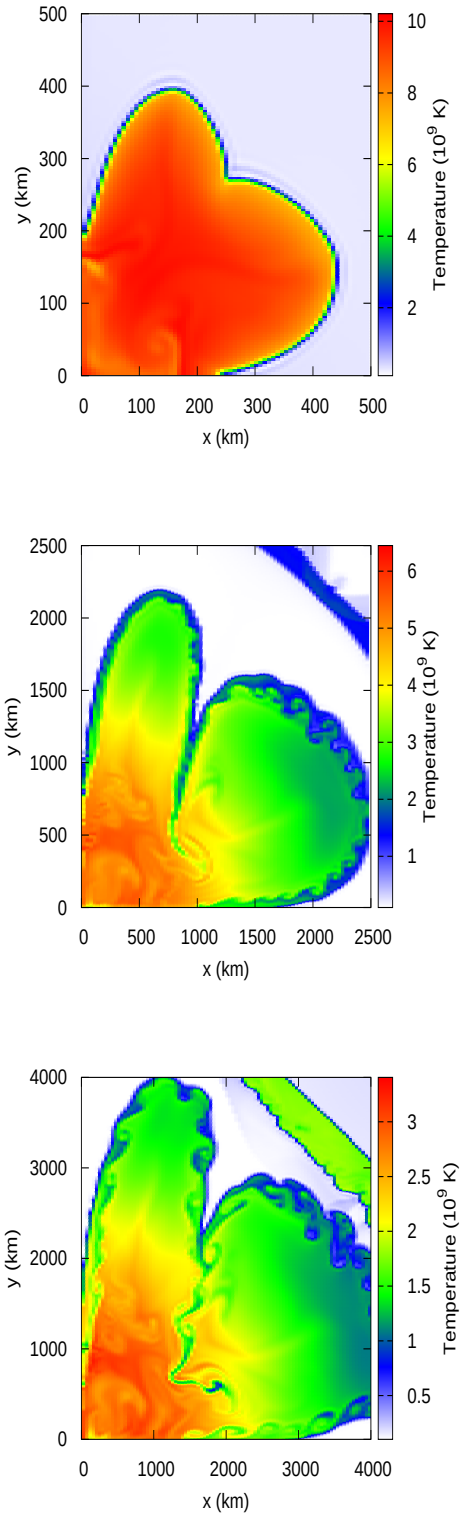

Figure 10. The temperature colour plot of the Model b1b-09950-N at 0.5, 1.0 and 1.25 s of the simulations. The hot region also represents the region being burnt by the ONe deflagration.

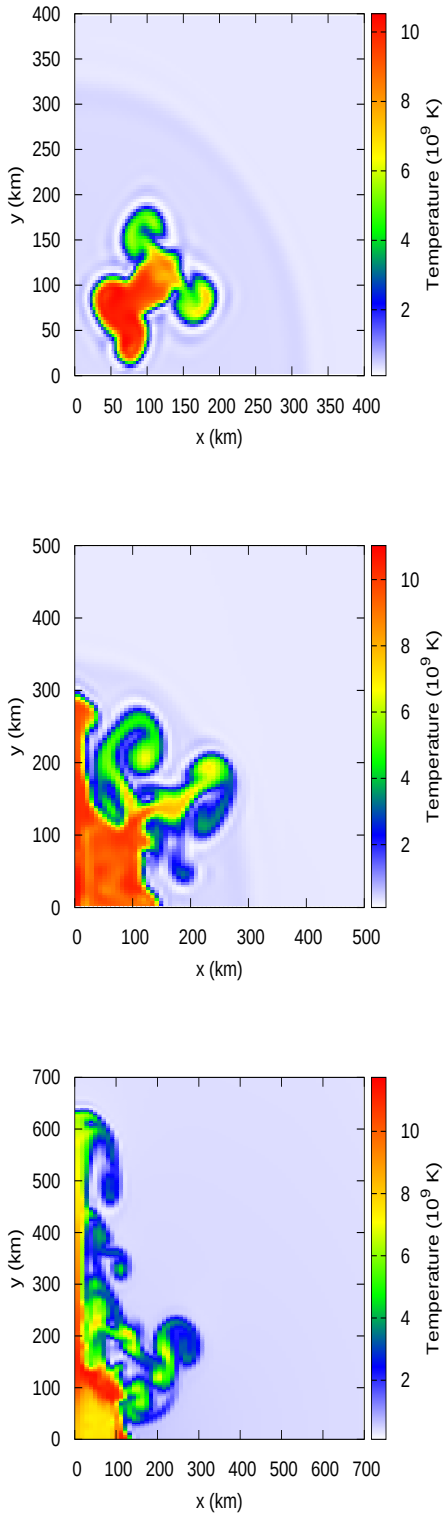

Figure 11. The temperature colour plot of the Model b1b-09950-N-Lam at 0.4, 0.8 and 1.2 s of the simulations. The hot region also represents the region being burnt by the ONe deflagration.

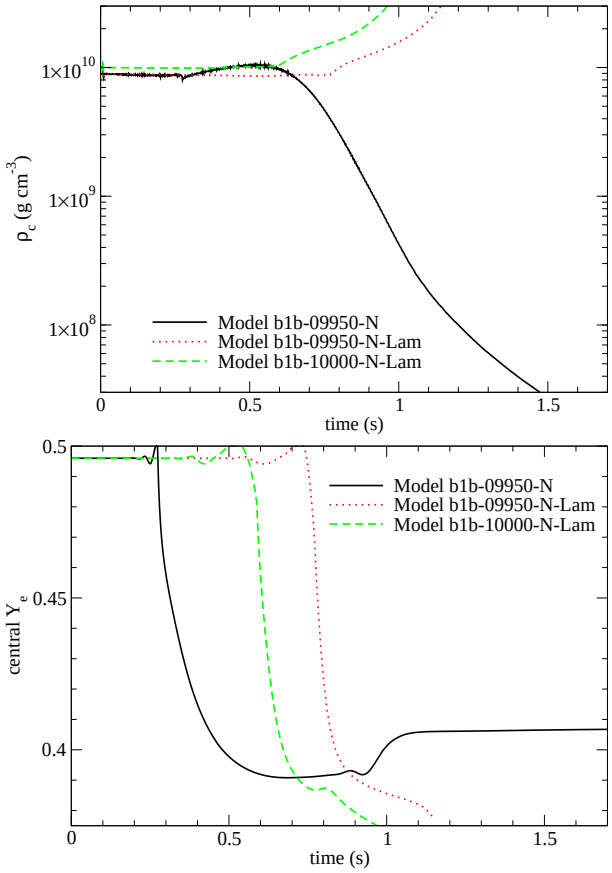

Figure 12. (upper panel) The central density against time for Models b1b-09950-N, b1b-09950-N-Lam, b1b-10000-N-Lam. (lower panel) Similar to the upper panel but for the central Y_e for the same set of models.

anchored at the core, where one can see a hot core of size 150 km. After that, core does not grow in a visible size. However, there is a hot flow along the rotation axis. This is the mentioned enhancement due to Rayleigh-Taylor instability along the symmetry boundary. However, this enhancement does not affect the results as we checked that the burned mass does not increase significantly. Within a further 0.2 s, the core directly collapses.

We further study their evolution by the stellar quantities. In the upper panel of Figure 12 we plot the central density against time for Models b1b-09950-N-Lam, b1b-09975-N-Lam, b1b-10000-N-Lam. For comparison we also plot the value for Model b1b-09950-N. The central densities of Models b1b-09950-N and b1b-09950-N-Lam are the same before $t = 0.4$ s, when the flame has not arrived the core. Once it reaches the core, namely at $t = 0.4$ s for Model b1b-09950-N and at $t = 0.8$ s for Model b1b-09950-N-Lam, they deviate from each other. Both models show an increase in central density due to the softening effect by electron capture. However, for Model b1b-09950-N, the central density starts to drop beyond $t = 0.6$ s, showing that the turbulent flame has released sufficient energy to support against the inward flows. On the other hand, in Model b1b-09950-N-Lam, the increase in central density leads to the collapse where there is no sign for the core to reach a temporary equilibrium. A similar evolution can be seen for Model b1b-10000-N-Lam. After $t = 0.8$ s where the flame reaches the core, the increment in central density further triggers the collapse.

In the lower panel of Figure 12 we plot similar to the upper panel but for the central Y_e. After the flame has reached the core, which can be noted by the sudden drop of Y_e, the electron capture of expanding b1b-09950-N slows down at $t \approx 0.5$ s at the value 0.3. It later returns to a high value as it starts to mix with higher Y_e material in the outer zone. On the other hand, the Y_e does not reach any equilibrium value once the core is burnt. The effective electron capture rate is slowed down at $t = 0.9$ s. Model b1b-10000-N-Lam also has a similar pattern. But it shows a short equilibrium Y_e at 0.8 s, showing that the center does not prefer to collapse right away; while the outer matter, which continues to flow inwards, as implied by the growth of the central density, triggers further electron capture which makes the collapse.

Then we compare the evolution of the two models by plotting the radial profiles. The radial profiles are obtained by doing an angular average of the related quantities. This allows us to compare more directly how the ONeMg core responses under different types of flame, and furthermore how the ONeMg core looks dynamically when it expands or collapses.

In Figure 13 we plot the density, temperature and Y_e radial profiles for the Model b1b-09950-N in the left, middle and right panels respectively. We plot in Figure 14 similar to Figure 13 but for the Model b1b-09950-N-Lam.

Model b1b-09950-N is an expanding model. The central density of the star quickly drops by two orders of magnitude in ≈ 1 s. However, the monotonic structure of density in the inner part of the core does not change throughout the event. This shows that the deflagration we modeled is quiet enough to suppress acoustic sound generation. On the other hand, there is almost no change in the profile in Model b1b-09950-N-Lam, which is a collapsing model. The star shows to contract homologously until the end of simulation.

For Model b1b-09950-N, the temperature profiles show more feature compared to the density. The off-center burning allows the temperature peaks at 100 and 500 km at $t = 0.5$ and 1.0 s. When the star begins its expansion, the off-center temperature peak is smoothed out. Besides that, the initial injection of flame creates

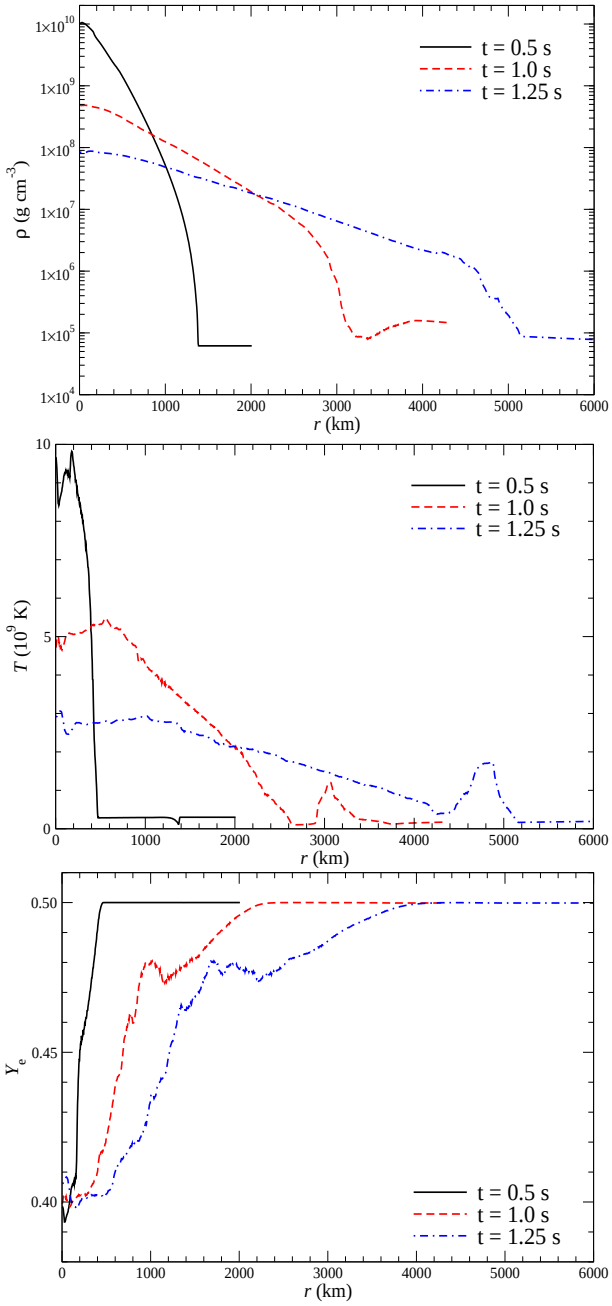

Figure 13. (left panel) The angular averaged radial density profiles of Models b1b-09950-N at t = 0.5, 1.0 and 1.25 s. (middle panel) Similar to the left panel but for the temperature profiles. (right panel) Similar to the left panel but for the Y_e profiles.

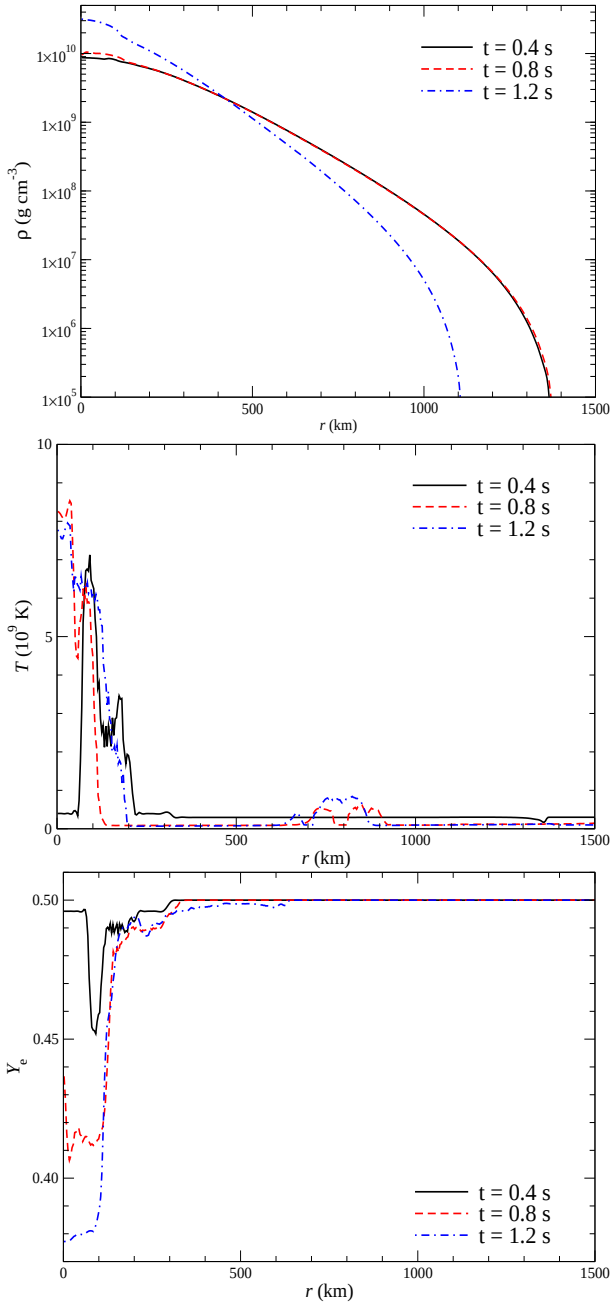

Figure 14. (left panel) The angular averaged radial density profiles of Models b1b-09950-N-Lam at t = 0.5, 1.0 and 1.25 s. (middle panel) Similar to the left panel but for the temperature profiles. (right panel) Similar to the left panel but for the Y_e profiles.

a small pulse which heats the near-surface matter and creates a small temperature bump at 3000 and 5000 km at 1.0 and 1.25 s. For Model b1b-09950-N-Lam, the flame is still off-center at 0.4 s. A small temperature bump is observed at $\sim$ 700 km due to the perturbation of initial flame. Until the end of the simulation, the high temperature region ($T > 3 \times 10^9$ K) is confined in the innermost 200 km.

For Model b1b-09950-N, the initial electron capture is confined to the innermost 200 km. Accompanying with the expansion, the shape of Y_e profile is frozen beyond 1.0 s, where expansion elongates the profile later on. For Model b1b-09950-N-Lam, the slow "laminar" allows

more transport of Y_e before rapid electron capture takes place. The electron captures at $t = 0.8$ and 1.2 s are localized at the innermost 100 km and carry on until the end of simulation.

3.7. *Effects of Pre-Runaway Time Lapse*

In our simulations, the initial flame we put is limited by the size of the resolution grid ($\sim$ 4 km). However, it is unclear whether the flame is triggered in this size, or at a size smaller than the grid resolution. In fact, in Timmes & Woosley (1992), the size of flame in mass can be as small as (10^3 - 10^{17} g), depending on the local temperature, such that the runaway can carry out spontaneously. This means that the initial runaway can have a size much smaller than the typical resolution ($\sim$ km) when the first nuclear runaway starts. Therefore, there can be a time lapse between the "first" nuclear runaway and the flame structure we used. The time lapse allows the Y_e inside the initial runaway be different from the original one initially. To account for this lapse, we prepared some more models with a much smaller $c3$ flame (for a few grids in order to make the flame shape well resolved by the level-set method). The flame is then allowed to only expand self-similarly until it becomes the shape of a bc3 flame. After that the fluid advection of the flame is resumed. Meanwhile, all nuclear reactions, such as photo-disintegration of ^{56}Ni into ^{4}He, and electron capture, can proceed. The process continues until the flame becomes the size of the $c3$-flame we used in previous simulations. At that point, we allow the flame to follow fluid advection.

In this series of model, we change the initial size of the flame from 25 % to 75 % of the original flame used in the $c3$ Model series. We choose the largest flame model because we want to contrast the effects of time lapse in the initial laminar phase. Again we use the bc3 as the template because it has the size sufficiently large such that we can construct similar flame structure of smaller size for comparison.

In Figure 15, we show the colour plot of the Y_e of the Model c3-09950-N-B050 at the moment we allow the deflagration to follow fluid motion when the flame reaches the required size. It takes about 125 ms for the flame to reach from half of its size (about 60 km) to the current size. The $c3$-flame is chosen as described above. Near the flame surface, as the weak interaction is slow, most matter remains to have its original Y_e. Around $r = 80$ km, the Y_e quickly drops from 0.50 to $\sim$ 0.44. Within the innermost 40 km, the Y_e can drop as low as 0.40 - 0.42.

In the upper panel of Figure 16 we plot the evolution of central density against time for Models bc3-09950-N,

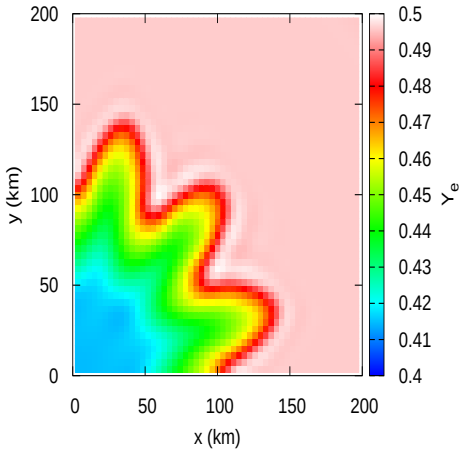

Figure 15. The Y_e colour plot of Model c3-09950-N-B050 by including the laminar propagation phase.

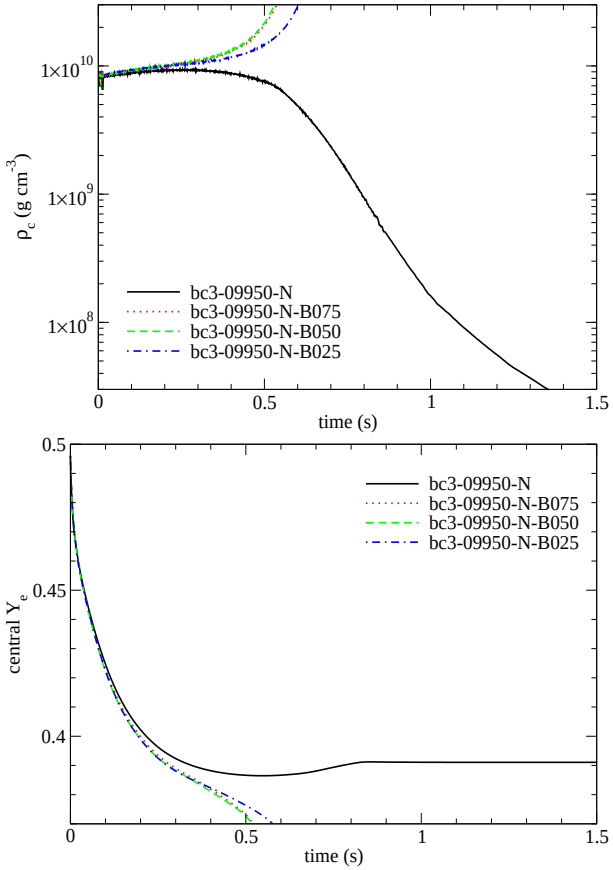

Figure 16. (upper panel) Similar to the upper panelThe evolution of central density against time for Model bc3-09950-N, bc3-09950-N-B070, bc3-09950-N-B050 and bc3-09950-N-B025. (lower panel) Similar to the upper panel but for the central Y_e for the same set of models.

bc3-09950-N-B075, bc3-09950-N-B050 and bc3-09950-N-B025. Model bc3-09950-N explodes while the other three models collapse. At the first 0.2 s, all four models show a similar ρ_c evolution. However, beyond that time point, the density in the three models are slightly higher, which leads to its later collapse at 0.5 - 0.6 s.

In the lower panel of Figure 16 we plot similar to Figure 16 but for the central Y_e. The three collapsing models show a qualitatively similar pattern as those in previous sections. But they all share a lower Y_e compared to the exploding model bc3-09950-N. This is related to the difference in the relaxation of the initial flame by isobaric expansion.

These contrasting results show that the ONeMg core evolved from stellar evolutionary model is likely to collapse into a neutron star and forms ECSN, but the exact details still strongly depend on the pre-runaway scenario, where the electron captures in the sub-grid scale are important for the initial Y_e profile and also its subsequent dynamics. We also remark that despite the flame structure of flame c3-09950-N and bc3-09950-N-B025 being the same, they are not identical because bc3-09950-N-B025 has more time for electron capture during the enforced laminar flame phase. Also the frozen flame shape at the laminar phase in Model bc3-09950-N-B025 allows different turbulence energy distribution when the flame can propagate freely, when compared with the Model c3-09950-N.

4. DISCUSSION

4.1. *Global Properties of ONeMg Core*

In previous sections we have compared the final evolution of ONeMg core with different input physics. We find that the initial central density, flame position and flame speed are important to pin down this final fate. In this section, we summarize the models by building a phase diagram of these models.

In Figure 17 we plot the phase diagram of the collapse-expand bifurcation of our models with the initial flame position and the initial central density as the $x-$ and $y-$coordinates. Two contrasting flame speeds, the default one and the reduced one, at an asymptotic value of 25 % of the default value, are shown. We mark the figure with two horizontal lines which characterize the runaway density using the Ledoux and Schwarzschild criteria. Some models are not computed but can be implied by the models of lower or higher ρ_c. The models above the Schwarzschild criterion collapse except for flame at 100 km. All models collapse at the initial central density using the Ledoux criterion.

By examining the distribution of "C" in the diagram, we find that the majority of models still collapses into a NS. The role of initial flame position plays a primary role in the transition and the flame speed plays a secondary role. The transition density increases when the flame position increases. However, comparing models with different flame speed, the transition density does not always change, depending on how close the model approaches the bifurcation point.

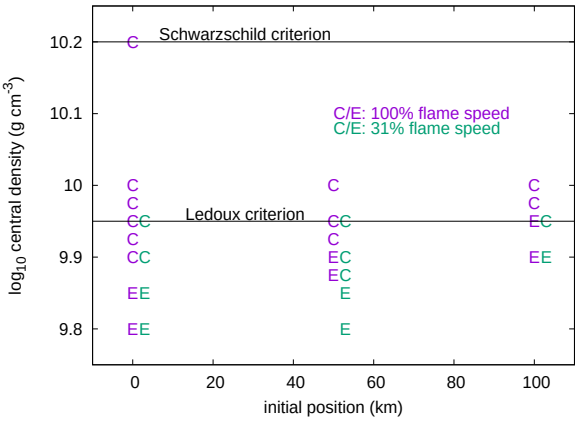

Figure 17. The phase diagram of the collapse-expand bifurcation for the models studied in this work. C and E correspond to the models which collapse and expand. The X- and Y-positions of the letter correspond to flame position (0, 50 and 100 km) and initial central density ($10^{9.8} - 10^{10.2}$). Models for two contrasting flame speeds at 100 % and 25 % are shown as the left one (purple font) and the right one (green font). The upper and lower lines correspond to the runaway densities predicted by Ledoux and Schwarzschild convection criteria.

This diagram demonstrates the diversity of the possible final outcome of ONeMg core, even when they are prepared in a very similar way in terms of mass, flame structure and flame position. From this, it suggests the necessity of future stellar evolutionary work in a better modeling of convective process prior to the runaway in order to pin down the exact final fate of the ONeMg core and a better understand of turbulent flame.

We also remark on the divergence of result among models with a c3, mc3 or bc3 flame. They demonstrate the importance of how the collapse depends on the global motion of the ONeMg core. We showed that model with a c3 flame has a longer time for the onset of collapse than that with a mc3 flame, while that with a bc3 flame expands. The small c3 flame takes more time for the development of flame until global contraction is triggered. On the other hand, the larger mc3 flame allows more electron capture to take place in the matter. This triggers the global contraction faster.

4.2. *Comparison with Literature*

Since there is no explicit work in the literature except Jones et al. (2016) on ECSN, we compare the typical hydrodynamics results with theirs. In Table 3 we list the input physics and configuration used in their work and this work. Overlap in microphysics is attempted to make the comparison of results easier. However, some fundamental infrastructure, including the hydrodynamics solvers, equation of states and nuclear reaction schemes are different.

First we examine the threshold density for the expand-collapse bifurcation. Our models show that a central ignited flame has a transition density at $10^{9.9}$ g cm^{-3}, and increases from $10^{9.925}$ and $10^{9.975}$ g cm^{-3} when the flame distance from the center increases from 0 km to 100 km. In the 6 models presented in Jones et al. (2016) with a ρ_c at $10^{9.90}$, $10^{9.95}$ and $10^{10.2}$ g cm^{-3}, the first two models expand and the last one collapses. Given that they use a different flame structure ($\sim$ 100 flame bubbles with a total mass $\sim 10^{-3} M_\odot$ burnt) at the beginning, our results agree qualitatively with theirs by considering their representative flame distance, initial burnt mass and central densities. Also, their (our) model with $\rho_{c,ini} = 10^{10.2}$ g cm^{-3} has a collapse time around 0.3 (0.26) s, which also agrees with each other (See for example Figure 7 for the evolution of central density).

Then we compare the flame morphology. In their work, they show the flame structure in Figure 6 and the cross-section cut in Figure 7. We compare this with our results in Figure 21. The outburst of flame in the spherical shape with Rayleigh-Taylor instabilities induced small-scale sub-structure can be seen. It resembles with Figure 6 in their work that the structure is spherical with many small-scale wrinkles on the surface. Because our model has a coarser resolution compared to their work, the flame structure in our model shows fewer sub-structure as theirs.

At last we compare the time evolution of turbulent flame. In Figure 18 we plot the speed of sound, laminar flame speed and turbulent flame speed of the Model c3-09850-N. The data is taken on the grid point which is actively burning by deflagration. At the beginning, laminar flame is dominant because we assumed a ONeMg core in hydrostatic equilibrium. We note that in their work the turbulent flame speed is slower than ours. It is because in the formalism from Pocheau (1994), the minimal turbulent flame speed is always the laminar flame speed. We estimate that the turbulence velocity is comparable with the flame speed when $t < 0.2$ s.

The turbulent flame speed quickly exceeds the laminar flame and reaches an equilibrium value of about a few percents of the speed of sound. This figure can be compared with Figure 4 in Jones et al. (2016) G13 model but with three differences. First, they used three-dimensional Cartesian coordinates, and we use two-dimensional cylindrical coordinates. Their three-dimensional modeling may allow more complex flame structure in the simulation. The higher dimensional allows more flexible choice of initial flame with less concern of enhancement by a particular boundary condition. Second, the sub-grid scale (SGS) model is based on the formalism in Schmidt et al. (2006) while ours is based on the scheme in Niemeyer et al. (1995). Both models belong to the class of one-equation model but with a different closure. Third, their models start from a number of off-center bubbles, while, due to symmetry, we choose a centered flame as the initial flame structure. Our "three-finger" structure helps to enhance the turbulence by the initial asymmetrical flow. This allows our model to reach the turbulent regime faster than theirs, resulting in more vigorous nuclear burning. On the other hand, the bubble structure, where bubbles are geometrically isolated at the beginning, makes the generation of turbulence slower because of the initially isotropic expansion of the bubble. Even with very different sub-grid turbulence models, the results are qualitatively similar, such as the asymptotic value and the range of turbulent flame speed found in the simulation. One major difference is the time when turbulence becomes saturated owing to our choice of initial flame. We choose the $c3$ flame as done in Reinecke et al. (1999). At last, in our simulations, the reflective inner boundaries of both planes can create boundary flows, which can also enhance the SGS turbulence production. The above differences imply that direct comparison of the previous work in the literature with ours is less encouraged. Future extension of our work in three-dimension and with similar flame structure and resolution, will provide more rigorous constraints on the collapse-expand transition boundary.

4.3. *Case for Failed-Collapse*

Here we discuss the properties of the exploding models, and then we analyze the possible nucleosynthesis signature of the exploding models. We analyze the thermodynamics history of one of the expanding models c3-09800-N by studying the tracer particles.

First we plot in Figure 19 $\rho_{\rm max}$ against $T_{\rm max}$ derived from the tracer particles in the simulations. The maximum density and temperature are defined by the maximum values experienced by the particles throughout its history from the onset of flame until expansion. The distribution is separated into three parts. The first part is a monotonic increasing trend at high $T_{\rm max} \sim 6 \times 10^9$ K. The second part is an approximately constant $\rho_{\rm max}$ at intermediate $T_{\rm max} = 3 - 6 \times 10^9$ K and

Table 3. Comparison of input physics and numerical setting between our work and those in Jones et al. (2016).

Physics component	Our work	Jones et al. (2016)
Numerical code	Leung et al. (2015a)	LEAFS
Dimensionality	2D	3D
Coordinates	Cylindrical	Spherical
Spatial discretization scheme	WENO (5th order)	PPM (3rd order)
EOS	Helmholtz	Individual prescription
Sub-grid turbulence	Niemeyer et al. (1995)	Schmidt et al. (2006)
Energy scheme (in Hydro)	3-step burning with NSE	1-step burning with NSE
Hydro Isotope network	7	5
Flame capturing scheme	Level-set methods	Level-set methods
Post-processing Isotope network	495	N/A
Electron capture rate	Extension of Seitenzahl et al. (2010)	Extension of Seitenzahl et al. (2010)
Nuclear reaction rate	Langanke & Martinez-Pinedo (2001)	N/A

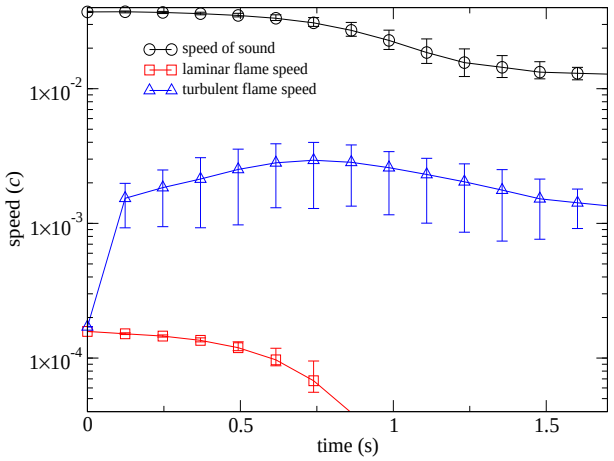

Figure 18. The speed of sound, laminar flame speed and turbulent flame speed for the Model c3-09850-N shown in Figure 3. For all velocities, the lines stand for the mass-averaged values from the grids where the flame surface can be found. The error bars show the maximum and minimum flame speeds found in the simulations at those time instants.

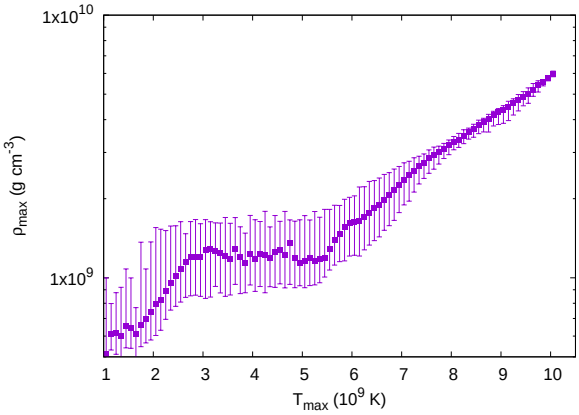

Figure 19. The maximum density $\rho_{\rm max}$ and maximum temperature $T_{\rm max}$ experienced by the tracer particles for the Model c3-09800-N. The error bars stand for the range of $\rho_{\rm max}$ of the tracers fo the same bin of $T_{\rm max}$.

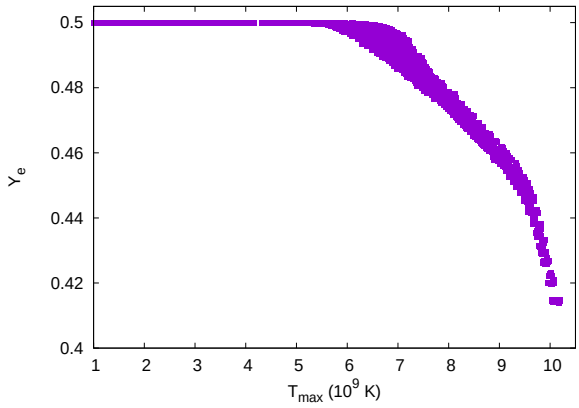

Figure 20. The final $Y_{\rm e}$ and maximum temperature $T_{\rm max}$ experienced by the tracer particles for the Model c3-09800-N.

the third part is another monotonic increasing trend at low $T_{\rm max} < 3\times10^9$ K. The tight relation for high $T_{\rm max}$ is consistent to the typical Type Ia supernova under pure turbulent deflagration. The subsonic deflagration wave does not generate any strong sound wave which can increase the spread of $T_{\rm max}$ for a given $\rho_{\rm max}$. Also most inner part of the core is burnt at the same time by the centered flame. On the other hand, for intermediate $T_{\rm max}$, the flame becomes aspherical that the fluid can experience different level of time lapse when the flame arrives the matter for the same initial density. At low $T_{\rm max}$, it shows the trend when the flame is quenching, which occurs at $\rho \sim 10^9$ g cm^{-3}. The value is higher than that for C+O matter because the typical energy release for burning of O+Ne matter is lower.

Then we plot in Figure 20 the Y_e distribution of the tracer particles as a function of ρ_{max}. The distribution consists of two parts. For the tracer particles which experienced electron capture ($T > 5 \times 10^9$ K), the final Y_e drops when T_{max} increases. The lowest Y_e experienced by the particles at highest temperature at $\sim 10^{10}$ K can be as low as 0.41. A small spread can be seen for particles close to the NSE transition temperature. Again, this is related to the aspherical nature of flame when flame propagates.

Since the electron capture rate is much slower than the dynamical timescale, the final Y_e determines the isotopes in the ejecta. At such low Y_e, neutron-rich isotopes such as ^{48}Ca ($Y_e = 0.41$), ^{54}Cr ($Y_e = 0.42$), ^{60}Fe ($Y_e = 0.43$), and ^{64}Zn ($Y_e = 0.47$). (The relative Y_e for Zn is high but the high entropy environment enhances the formation of this particular isotope compared to the Type Ia SN counterpart. See e.g. Wanajo et al. (2018); Jones et al. (2019).) As discussed in Nomoto & Kondo (1991); Woosley (1997), these isotopes are not well produced in ordinary SNe. These isotopes, if ejected, will provide tight constraints on the relative rate to other types of supernovae.

We do not attempt to do the nucleosynthesis as in our previous work because a longer time after explosion ($\sim$ 10 s) is necessary in order to distinguish the tracers which are ejected and tracers which fall back to form the remnant. Without this information, the final yield can overestimate the final masses for iron-peak elements, which are more likely to fall back during its outward expansion and transport of momentum from the core to the envelope.

Furthermore, after the expansion takes place, the ONeMg core ejects its matter partially. The ejecta may contain elements from both its ONe-rich fuel and Fe-rich ash of the ONeMg core. The remained matter will become a lower-mass remnant. In Jones et al. (2016) a typical mass of $\sim 1.2 M_\odot$ of remnant is recorded. The lower mass remnant may coincide with the low-mass SiFe-rich white dwarfs observed (Raddi et al. 2018). We remark that in Jones et al. (2019) they further computed the nucleosynthesis yield using a large nuclear reaction network. The comparison of our nucleosynthesis yield with theirs, and a detailed analysis as a function of progenitor mass and flame structure will be our future work.

4.4. *Conclusion and Future Work*

In this article we study the evolution of oxygen-neon-magnesium (ONeMg) core using the two dimensional hydrodynamics simulations. We used the typical ONeMg core based on stellar evolution models and extended it to different masses. We followed the ONe deflagration phase to examine at which conditions will the core collapse into a neutron star.

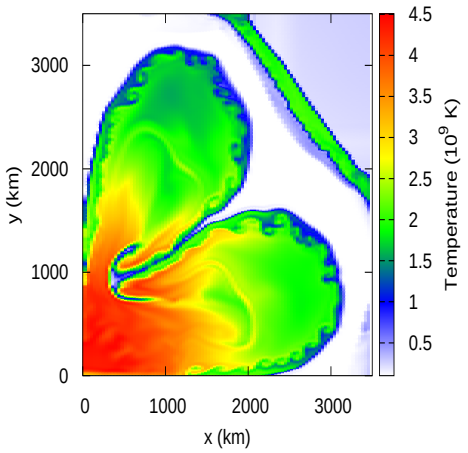

Figure 21. The temperature profile of the Model bc3-09950-N at 1 s of the simulation. Notice that the flame is highly irregular with the signature of Rayleigh-Taylor instabilities and Kelvin-Helmholtz instabilities.

We surveyed ONeMg core models of various configurations. This includes a central density of $10^{9.80} - 10^{10.20}$ g cm^{-3}, and different flame structure of mass from $10^{-4} - 10^{-2}$ $M_\odot$ in a centered or off-centered ignition kernel. We also explored the effects of input physics, which include the general relativistic effects, turbulent flame speed formula and treatment of the laminar deflagration phase. We find that except the general relativistic effects, the later two input physics are highly influencing to the collapse condition. The exact transition density depends on the input physics but we find that the ONeMg core can collapse with an initial central density ranging $10^{9.90-9.975}$ g cm^{-3}. This is consistent with the current picture of stellar evolution that the ECSN of the 8 - 10 $M_\odot$ could be the origin of the lower-mass branch of neutron star population.

We study how the input physics affects the bifurcation condition of the ONeMg core. Besides the sensitivity of the model to the initial mass as reported in the literature, for the models with the same central density, a centered flame favors the collapse scenario. Slower flame (laminar flame or less effective turbulence models) also favors the collapse scenario. A pre-conditioned flame is also favorable to the collapse branch. However, relativistic corrections in gravity do not play a main role to the evolution of this part.

We have presented a phase diagram for the collapse-expansion bifurcation for models with a range of central

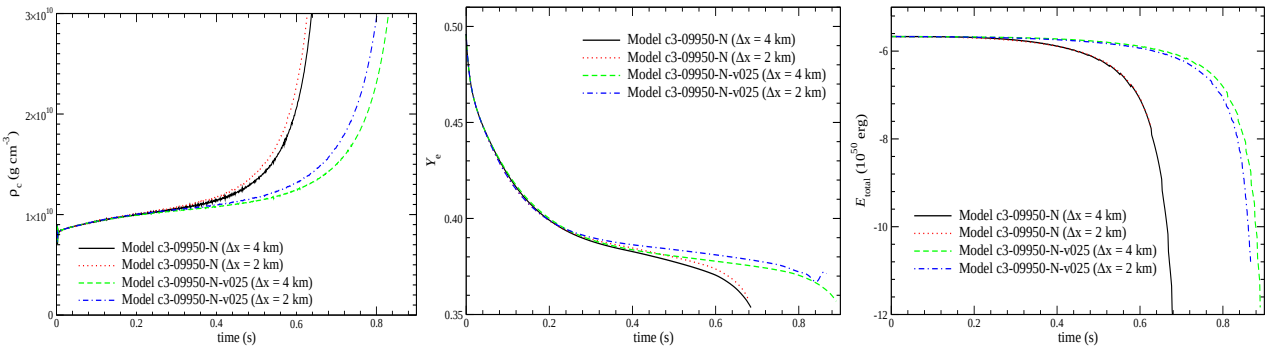

Figure 22. (left panel) The central density for the Model c3-09950-N, c3-09950-N-fine, c3-09950-N-v025 and c3-09950-N-v025-fine. (middle panel) Similar to the left panel but for the central Y_e. (right panel) Similar to the left panel but for the total energy.

densities, flame positions and turbulent flame speeds. We studied the thermodynamics history of the ECSN and discussed its nucleosynthesis implications. We also carried out a detailed comparison of our models with the representative models in the literature. Our results suggest that more careful treatments in the pre-runaway convections in the stellar evolution of ONeMg core, turbulent flame modeling, and the mapping from the stellar evolutionary models to hydrodynamics simulations will be necessary in order to pin down the final fate of SAGB star after electron-capture-induced nuclear runaway has started.

5. ACKNOWLEDGMENT

This work was supported by World Premier International Research Center Initiative (WPI), MEXT, Japan, and JSPS KAKENHI Grant Numbers JP26400222, JP16H02168, JP17K05382 We acknowledge the support by the Endowed Research Unit (Dark Side of the Universe) by Hamamatsu Photonics K.K. We thank the developers of the stellar evolution code MESA for making the code open-source. We thank F. X. Timmes for his open-source micro-phsyics algorithm including the Helmholtz equation of state subroutine, the torch nuclear reaction network designed for an arbitrary choices of isotopes, the seven-isotope nuclear reaction network. We also thank Ming-Chung Chu for the initial inspiration of building the hydrodynamics code. We also thank H. Shen for her open source equation of state for the nuclear matter. We thank Christian Ott and Evan O'Connor for the EOS driver for reading the HShen EOS and their open source data for the parametrized electron capture value before bounce. We thank Zha Shuai for his discussion of the preliminary results of his pre-runaway models.

APPENDIX

A. RESOLUTION STUDY OF THE CODE

In this work we have performed a number of simulations using the same resolution at ~ 4 km. It has been a matter of issue how the results depend on the resolution, especially in simulations of this type which rely on input physics involving grid size as the input parameter (e.g. sub-grid turbulence). To understand the validity of our results, we attempt to rerun the benchmark model (Model c3-09950-N) and its counterpart with a slower flame speed (Model c3-09950-N-v025) in a finer resolution at ~ 2 km. We denote the this model as Model c3-09950-N-fine and Model c3-09950-N-v025-fine respectively. We also do the comparison for the slower flame because the slower flame takes longer time for the collapse to occur. This provides more time for the propagation of the flame, which may amplify the resolution effects.

In the left panel of Figure 22 we plot the central density evolution of the two models. The evolution of the first 0.5 s of the Models c3-09950-N and c3-09950-N-fine is almost identical. Similar pattern can be seen for the pair of Models c3-09950-N-v025 and c3-09950-N-v025-fine. However, the models deviate from each other where the central density of the finer model grows faster. Despite that, both models stop at a time of ~ 0.62 and 0.82 s with a difference $\sim 1\%$, when the central density reaches the threshold defined in the code.

In the middle panel of Figure 22 we plot the central Y_e evolution for the four models. The central Y_e of the two pairs are very similar to each other at early time. There is a small bump for Model c3-09950-N-v025-fine, which may be originated from resolved mixing with outer meshes, which have a higher Y_e in general.

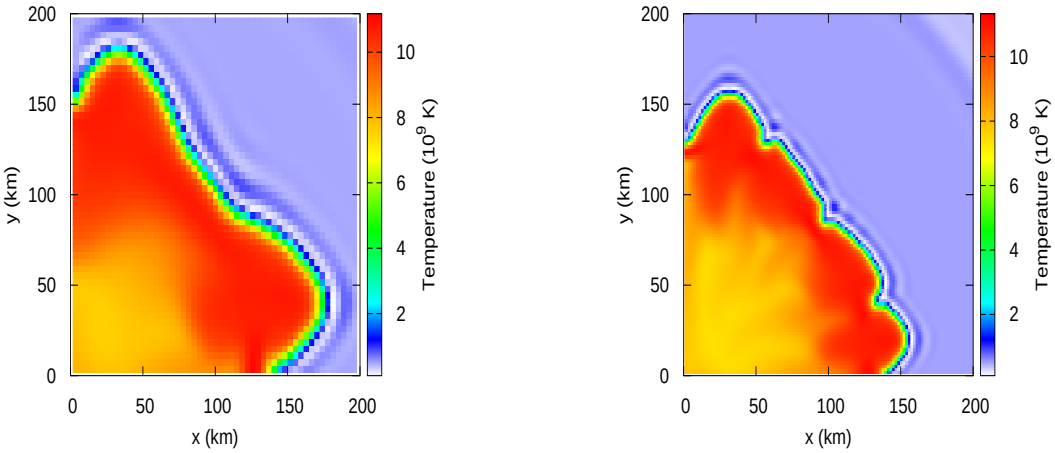

Figure 23. (left panel) The temperature colour plot of the Model c3-09950-N-v025 at 0.75 s after the deflagration has started. (right panel) Similar to the left panel but for the Model at c3-09950-N-v025-fine.

In the right panel of Figure 22 we plot the energy evolution for the two comparison models. The model pair based on Model c3-09950-N-v025 shows very similar evolution except near the end. Both models show a sharp drop of total energy near the end of simulation due to the neutrino loss and energy loss by electron captures. The model with a finer resolution shows an earlier drop in the energy consistent with the central density evolution. On the contrary, the energy curves of the model pair based on Model c3-09950-N almost overlap with each other.

We can see from the results that a finer resolution in general allows faster energy production. This suppresses the effects from electron capture and hence the rate of contraction. To further understand the role of resolution size in our simulations, we plot in left and right panels of Figure 23 the flame structure of the two models at 0.75 s after the simulations have started. The flame structure of the two models are of similar shape. The initial "three-finger" structure is smoothed out due to the electron capture effects. The model with a higher resolution shows more features on the front than the lower resolution. However, the flame size is slightly larger for the lower resolution model by 20 %. The core cooled by electron capture is on the contrary smaller in the same model. Such difference can attribute to the different contraction rate, where the lower resolution model, due to a more extended flame, needs more time for accumulating sufficient matter for the final collapse. Despite the difference, the flame structure shows that the current resolution can produce very coherent results, despite a more rigorous proof will need further smaller Δx to verify the convergence.

B. POSSIBLE OBSERVATIONAL SIGNALS FOR THE COLLAPSING MODEL

In this section, we estimate the following evolution for models which collapse into a neutron star. We remap our models from the two-dimensional cylindrical grid to the one-dimensional spherical grid by doing an angular average. Then we carry out one-dimensional hydrodynamics simulations from the collapse until bounce occurs.

In Table 4, we list the input physics for doing the 1D modeling in the collapse phase. In the 1D simulation, we use the same WENO 5^{th} order shock-capturing scheme and the 3-step 3^{rd} order NSSP RK scheme for spatial and temporal discretization. For the EOS, we use the HShen EOS (Shen et al. 1998), which is based on the relativistic mean-field model to describe the homogeneous phase of matter. The table includes extension with the Thomas-Fermi approximation to describe the inhomogeneous matter composition. The parameter for the incompressibility of nuclear matter is 281 MeV and the symmetry energy has a value of 36.9 MeV. Before bounce occurs, we use the parametrized neutrino transport scheme (Liebendoerfer 2005). This scheme treats the electron capture as the only neutrino source and simplifies the neutrino transport by only including an instantaneous absorption/emission. The neutrino also affects the hydrodynamics through its pressure in the neutrino-opaque region as an ideal degenerate Fermi gas. To estimate the expected electron capture at high density, we use the fitting table in Abdikamalov et al. (2010), which contains the Y_{e} as a function of density. The electron fraction of the matter is instantaneously converted to the value given by the table, where the net change of electron capture is treated as neutrino source. After bounce, we switch

Table 4. The input physics and the choices of physics models in simulations.

Input physics	Physics model
Spatial discretization	$5^{\rm th}$ order Weighted Essentially Non-Oscillatory Scheme (Barth & Deconinck 1999)
Time discretization	5-step $3^{\rm rd}$ order Non-Strong Stability Preserved Runge-Kutta Scheme (Wang & Spiteri 2007)
Baryonic matter EOS	HShen EOS (Shen et al. 1998)
Pre-bounce electron capture	Fitting table from direct Boltzmann transport (Dessart et al. 2006; Abdikamalov et al. 2010)
Pre-bounce neutrino transport	Parametrized neutrino transport (Liebendoerfer 2005)
Post-bounce neutrino transport	Advanced leakage scheme (ALS) (A. Perego 2016)

to the Advanced Leakage Scheme (A. Perego 2016). This scheme can be regarded as the extension of the leakage scheme (Rosswog & Liebendoerfer 2003), but is a simplified scheme of the Isotropic Diffusion Source Approximation (IDSA) (Liebendoerfer et al. 2009). It is because this scheme treats the neutrino number fraction and mean energy as independent variables as in IDSA. But in evolving to the new state, in the neutrino sector, it always assumes the new state inclines towards to the diffusion limit in the optically thin zones or the trapped limit in the optically thick zones. This guarantees that the scheme can approach asymptotically to a solution for an arbitrary timestep. This can bypass the difficulty of finding a new state in the original version of IDSA where occasionally no solution is found in zones where rigorous motion or discontinuities exist. In our simulations, we use 10 energy bands of neutrino from 3 MeV to 300 MeV in a logarithmic increasing band size. Since we want to understand the general properties of how the collapse takes place, we include only ν_e and $\nu_{\bar{e}}$ in our calculation with only 2 absorption/emission channels and 4 scattering channels, namely:

$$n + \nu_e \leftrightarrow p + e^-, \tag{B1}$$
$$p - + \nu_{\bar{e}} \leftrightarrow n + e^+, \tag{B2}$$

for the absoption/emission, and

$$n + \nu_i \leftrightarrow n + \nu_i, \tag{B3}$$
$$p + \nu_i \leftrightarrow p + \nu_i, \tag{B4}$$
$$\alpha + \nu_i \leftrightarrow \alpha + \nu_i, \tag{B5}$$
$$\mathrm{ion} + \nu_i \leftrightarrow \mathrm{ion} + \nu_i \tag{B6}$$

respectively. We use the rate formulae given in Bruenn (1985). Pair neutrino and neutrino bremmstrahlung are not included in this calculation. But these processes are less important compare to the channels included, although we note that for a long term simulation such as neutron star cooling, these two channels gradually dominate over the first two absorption-emission channels.

Since the advanced leakage scheme does not include neutrino cooling, which is an important channel for the proto-neutron star to lose energy effectively after the neutrinosphere has been settled, we only run the simulations until ~ 200 ms after bounce, to extract the neutrino signals.

In the left panel of Figure 24 we plot the density profiles of one of the collapse models c3-10000-N at the beginning of the one-dimensional simulation, at bounce, 25 ms and 50 ms after bounce. At the beginning (end of the two-dimensional simulations in the deflagration phase), the core starts with a flat density profile. But the inner core first contracts to reach nuclear density due to the loss of pressure by electron capture. At bounce, a stiff core made of nuclear matter at density around 3×10^{14} g cm^{-3} is formed. The inner envelope shows a steep density gradient showing that it is still falling onto the neutron star. The outer envelope does not change much. At 20 ms after bounce, the neutron star core reaches an equilibrium state in density, while the accretion of matter of the inner envelope creates a layer outside the neutron star. At around 10^{12} g cm^{-3}, strong fluctuations of density appear due to the tension between the infalling matter from the outer envelope and the stabilized inner envelope. At 50 ms after bounce, the neutron star has a static state envelope about 200 km. The remained envelope has also contracted significantly to about 500 km, about half of its initial radius ≈ 1200 km. At 100 ms after bounce onward, no significant change in the

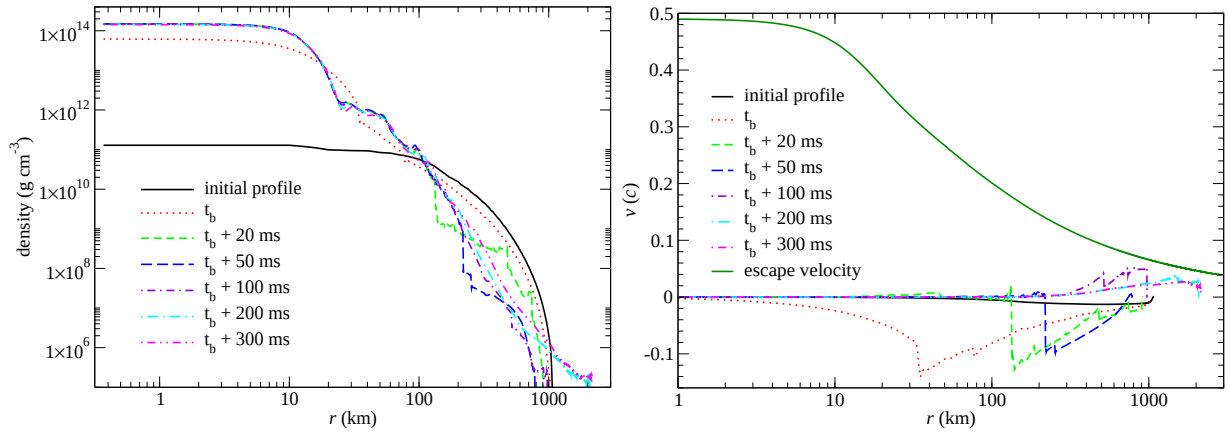

Figure 24. *(left panel)* The density profiles of the Model c3-10000-N at the start of simulation (the same profile as it ends in the 2-dimensional simulation), at the bounce, 20, 50, 100, 200 and 300 ms after bounce. *(right panel)* Similar to left panel, but for the velocity profiles.

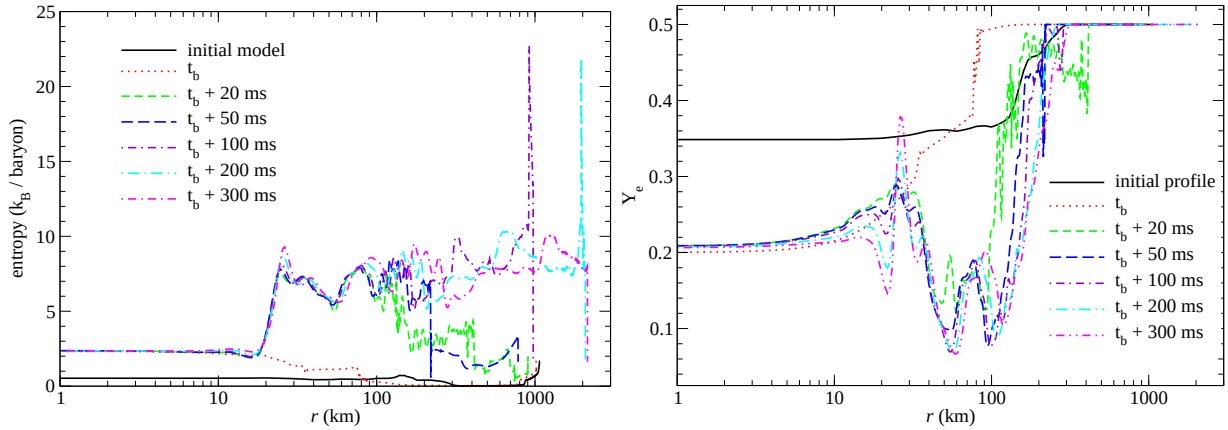

Figure 25. *(left panel)* The entropy profiles of the benchmark ECSN model at the beginning, at bounce, and at 20, 50, 100, 200 and 300 ms after bounce. *(right panel)* The Y_e profiles of the benchmark ECSN model at the beginning, at bounce, and at 20, 50, 100, 200 and 300 ms after bounce.

density profile of the neutron star up to 200 km. But there is still observable motion of the surface showing expansion. The cusps in the profiles also disappear.

In the right panel of Figure 24 we plot the velocity profiles for the same model similar to the left panel. At the beginning, the star is having a homologous contraction with a maximum velocity about 1.3×10^{-2} c at about 500 km. At bounce, we can see the a neutron star core close to static is formed with a size of about 15 km. Outside the neutron star there is an infalling envelope with a maximum velocity about 0.2 c. The infalling envelope preserves also the homologous velocity profile. Through shock heating, the material fallen on the neutron star quickly finds a hydrostatic equilibrium state. By examining the velocity profile at 20 ms after bounce, the bounce shock reaches about 100 km from the core, with a slightly lower infalling velocity about 0.16 c. There is outgoing matter in the profile at 50 ms after bounce. This shows that the shock has reached the region where density is low enough for the density gradient becomes large enough, so that the shock strength increases again when it propagates. The infalling velocity has decreased to $\approx 0.12c$. Once the accretion shock reaches the surface, since there is no further matter suppress to the expansion of matter, it creates a high velocity flow near the surface. Some has a velocity exceeding the escape velocity. Such ejecta is likely to make the event a dim and rapidly transient due to its high velocity and low ejecta mass. After the ejection of high velocity matter is ejected, the material becomes bounded.

In Figure 25 we plot the entropy profiles similar to Figure 24. At the beginning, the whole star has almost a constant entropy ≈ 0.5 k_B per baryon, except near the surface. This is related to the initial flame put in by hand. The initial flame perturbs the initial hydrostatic equilibrium of the star. At bounce, the whole star reaches a constant entropy

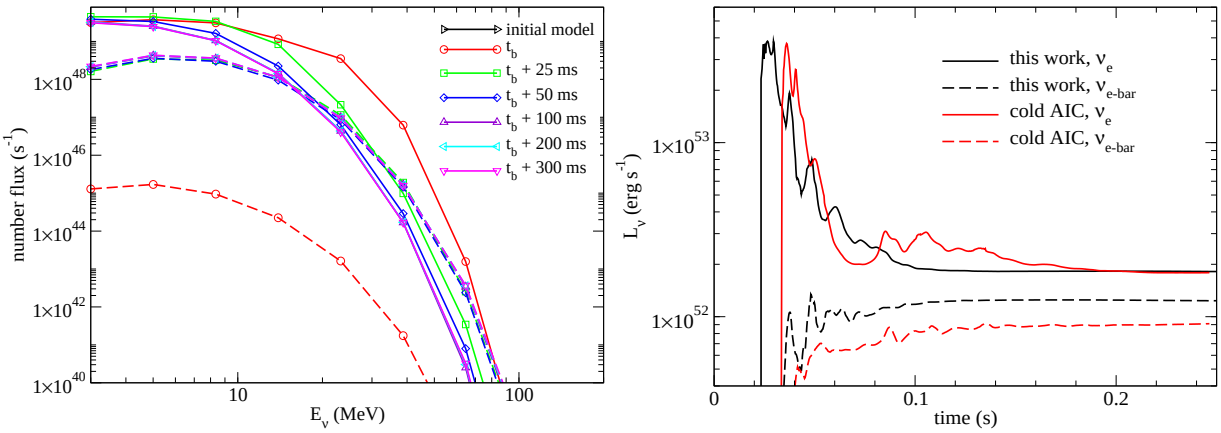

Figure 26. *(left panel)* Similar to the left panel but for the free streaming neutrino flux. The solid (dashed) line stands for the ν_e ($\nu_{\bar{e}}$) flux at 300 km from the NS core. *(right panel)* The ν_e and $\nu_{\bar{e}}$ luminosity for the Model c3-10000-N. The sample neutrino luminosity from the collapse of an AIC is included for comparison.

about 3 k_B per baryon. There is a cusp near the neutron star by the shock interaction. Similar to the velocity profiles, the quasi-static neutron star core has a constant entropy. At 20 ms, there is a significant rise of entropy to about 10 k_B per baryon in the newly accreted layer from 10 - 80 km. The high entropy region can be compared with the velocity profile, which is the region which comes to a rest after deposited on the neutron star surface. At 50 ms, the shock has reached 200 km and a high entropy domain forms up to about 110 km. This is consistent with the literature that the neutrino heating is essential in producing high entropy matter, which is supposed to be found in the ejecta. At 100 ms onwards, there is no significant change to the entropy profiles where a flat constant entropy zone is created in the envelope. At 100 ms after bounce, the ejecta has an entropy peak as high as $\sim$ 20 k_B per baryon.

In the right panel of Figure 25 we plot the Y_e profiles of the ECSN model similar to previous plot at the same time slice. The beginning Y_e profile is directly imported from the collapsing model in the main text. So, the core has reached a minimum of $\sim$ 0.35 and gradually increases at 100 km up to 0.45. At no electron capture takes place beyond 200 km, where the deflagration has not yet reached the matter. At bounce, the core Y_e reaches 0.2 and gradually increases to 0.35 at $\sim$ 60 km, and up to 0.5 at 80 km. The locally higher Y_e from 80 - 200 km is because of the advection of matter. The high Y_e matter falls inwards, but has not reached the density for electron capture, so locally it looks like the Y_e increases by itself. After bounce, the shock and the consequent neutrino interactions influence the Y_e distribution. The high temperature allows rapid neutrino emission, which creates a trough of Y_e from 30 - 100 km. Ripples of Y_e appears due to the finite partitioning of neutrino energy band. As the shock propagates outwards, at 100, 200 and then 300 ms, we can see the trough widens. Furthermore, the neutrinos, which diffuse outwards outside the neutrinosphere, smooth out the Y_e fluctuations created by acoustic waves right after bounce.

In the left panel of Figure 26 we plot the neutrino energy spectra of the same model similar to Figure 24. The number flux is taken at 300 km from the neutron star core. The number reaching the Earth can be scaled accordingly. There is no data for the initial model because no matter has reached nuclear density. At bounce, one can see the ν_e has already a spectrum comparable with the thermal spectrum. But the $\nu_{\bar{e}}$ spectrum is still extremely low. At 25 ms after bounce, ν_e has relaxed with a lower high energy ν_e since the neutrinosphere is in general farther from center, which has a lower temperature. The $\nu_{\bar{e}}$ has also settled down to a thermal distribution. At 50 ms, both types of neutrinos have reached an equilibrium distribution. There are more low energy ν_e but more high energy $\nu_{\bar{e}}$.

In the right panel of Figure 26 we plot the ν_e and $\nu_{\bar{e}}$ luminosity against time for the same model. The neutrino signal from an accretion induced collapse of a WD into a neutron star is also plotted for comparison. The accretion induce collapse assumes a simple collapse of a Chandrasekhar mass isothermal WD due to an initial reduction of Y_e. It can be seen that qualitatively the two models are similar. At the beginning, a strong pulse of ν_e is emitted. But as the neutrinosphere of different energy bands starts to form. The neutrino emission drops. After a few expansion of the envelope, it reaches an equilibrium value about 2×10^{52} erg s^{-1}. One minor difference is that the ONeMg case shows more oscillations than the cold AIC case. The $\nu_{\bar{e}}$ shows a similar behaviour. It has a much lower luminosity. Consistent to the literature, the first peak appears later than the ν_e peak, about 20 ms after. The ONeMg model has about 50 % higher $\nu_{\bar{e}}$ flux than the cold AIC model.

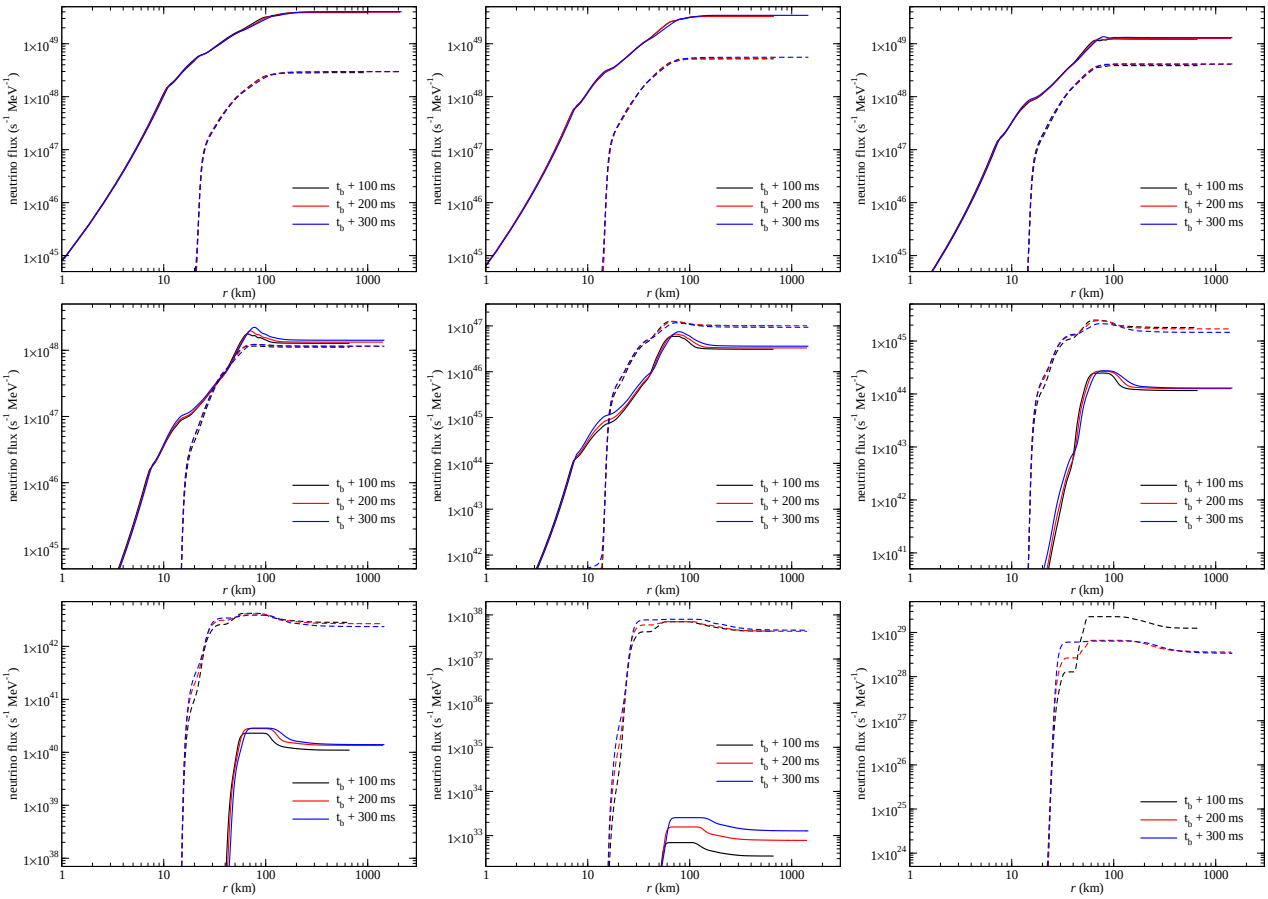

Figure 27. The ν_e (solid line) and $\nu_{\bar{e}}$ (dashed line) number flux profile at 100 (black), 200 (red) and 300 (blue) ms after bounce. The neutrino energy bands include 3, 5, 8, 14, 23, 39, 65, 108 and 180 MeV.

At last we plot at Figure 27 the neutrino number flux profile at 100, 200 and 300 ms after bounce for both ν_e (solid line) and $\nu_{\bar{e}}$ (dashed line). For low energy bands (3 MeV - 8 MeV), ν_e is the dominant species. They are mostly created just outside the NS, surface. No neutrino absorption can be seen and most neutrinos are produced within the innermost 100 km. On the contrary, $\nu_{\bar{e}}$ is completely not produced in the NS, and is gradually produced in the shock-heated matter outside the NS. Its number emission is at least one order of magnitude lower. However, as neutrino energy increases, the drop of ν_e number flux is faster than the drop of $\nu_{\bar{e}}$. It is because the creation of $\nu_{\bar{e}}$ is limited to places where positron can be freely formed. Notice that to create ν_e, the electron should have a chemical potential not only for the creation of itself, but also the mass difference between n and p ($\sim$ 1.2 MeV). At 20 - 100 km, the density has already drops below 10^{12} g cm^{-3}. This means the nucleons is no longer degenerate and thus it has a much lower chemical potential than those in the core. So, this leaves a strong cutoff in the high energy ν_e. On the other hand, the production of $\nu_{\bar{e}}$ is aided by the energy difference for the same origin. So, its drop in number flux is less steep than ν_e.

For a higher neutrino energy, more features can be observed. At 14, 23 and 39 MeV, both ν_e and $\nu_{\bar{e}}$ show a first increasing function up to 80 km and then slightly drop until 100 km. The change of ν_e is larger than that of $\nu_{\bar{e}}$, showing that more ν_e is absorbed. As a result, this explains the local bump of Y_e in the right panel of Figure 25.

For even higher neutrino energy (65, 108 and 180 MeV), the drops of ν_e becomes so rapid that it becomes irrelevant to the neutrino transport and the global neutrino flux. $\nu_{\bar{e}}$ also shows a similar feature but with lower strength. But they are also unimportant to the global neutrino population.

REFERENCES

A. Perego, R. M. Cabezon, R. K. 2016, ApJS, 223, 22

Abdikamalov, E. B., et al. 2010, Phys. Rev. D, 81, 044012

Arnett, D. 1996, Supernovae and Nucleosynthesis: An Investigation of the History of Matter from the Big Bang to the Present
Barth, T. J., & Deconinck, H. 1999, Lecture Notes in Computational Science and Engineering 9: High-Order Methods for Computational Physics (Springer)
Bell, J. B., Day, M. S., Rendleman, C. A., Woosley, S. E., & Zingale, M. 2004a, ApJ, 606, 1029
—. 2004b, ApJ, 608, 883
Bruenn, S. W. 1985, Astrophys. J. Suppl., 58, 771
Canal, R., & Schatzman, E. 1976, Astron. Astrophys., 46, 229
Dessart, L., Burrows, A., Ott, C., et al. 2006, Astrophys. J., 644, 1063
Doherty, C. L., Gil-Pons, P., Siess, L., Lattanzio, J. C., & Lau, H. H. B. 2015, MNRAS, 446, 2599
Fink, M., Kromer, M., Seitenzahl, I. R., et al. 2014, MNRAS, 438, 1762
Hashimoto, M., Iwamoto, K., & Nomoto, K. 1993, Astrophys. J., 803, 72
Hicks, E. P. 2015, Astrophys. J., 803, 72
Jones, S., Hirschi, R., & Nomoto, K. 2014, ApJ, 797, 83
Jones, S., Röpke, F. K., Pakmor, R., et al. 2016, A&A, 593, A72
Jones, S., Hirschi, R., Nomoto, K., et al. 2013, ApJ, 772, 150
Jones, S., Röpke, F. K., Fryer, C., et al. 2019, A&A, 622, A74
Karakas, A. I. 2017, Low- and Intermediate-Mass Stars, ed. A. W. Alsabti & P. Murdin, 461
Khokhlov, A. M., Oran, E. S., & Wheeler, J. C. 1997, ApJ, 478, 678
Kim, J., Kim, H. I., Choptuik, M. W., & Lee, H. M. 2012, Mon. Not. R. astr. Soc., 424, 830
Kitamura, H. 2000, Astrophys. J., 539, 888
Langanke, K., & Martinez-Pinedo, G. 2001, ADNDT, 79, 1
Langer, N. 2012, Ann. Rev. Astron. Astrophys., 50, 107
Leung, S.-C., Chu, M.-C., & Lin, L.-M. 2015a, Mon. Not. R. astr. Soc., 454, 1238
—. 2015b, Astrophys. J., 812, 110
Leung, S.-C., & Nomoto, K. 2017, in 14th International Symposium on Nuclei in the Cosmos (NIC2016), ed. S. Kubono, T. Kajino, S. Nishimura, T. Isobe, S. Nagataki, T. Shima, & Y. Takeda, 020506
Leung, S.-C., & Nomoto, K. 2018, ApJ, 861, 143
Liebendoerfer, M. 2005, Astrophys. J., 633, 1042
Liebendoerfer, M., Whitehouse, S. C., & Fischer, T. 2009, Astrophys. J., 698, 1174
Livne, E., & Arnett, D. 1993, ApJ, 415, L107
Long, M., Jordan, George C., I., van Rossum, D. R., et al. 2014, ApJ, 789, 103
Ma, H., Woosley, S. E., Malone, C. M., Almgren, A., & Bell, J. 2013, ApJ, 771, 58
Miyaji, S., & Nomoto, K. 1987, Astrophys. J., 318, 307
Miyaji, S., Nomoto, K., Yokoi, K., & Sugimoto, D. 1980, PASJ, 32, 303
Mochkovitch, R., & Livio, M. 1989, Astron. Astrophys., 209, 111
Nabi, J.-U., & Klapdor-Kleingrothaus, H. V. 1999, ADNDT, 71, 149
Niemeyer, J. C., Hillebrandt, W., & Woosley, S. E. 1995, Astrophys. J., 452, 979
Nomoto, K. 1982, Astrophys. J., 253, 798
—. 1984, Astrophys. J., 277, 791
—. 1987, Astrophys. J., 322, 206
Nomoto, K., & Hashimoto, M. 1988, PhR, 163, 13
Nomoto, K., Kobayashi, C., & Tominaga, N. 2013, ARA&A, 51, 457
Nomoto, K., & Kondo, Y. 1991, Astrophys. J., 367, L19
Nomoto, K., & Leung, S.-C. 2017a, Electron Capture Supernovae from Super Asymptotic Giant Branch Stars (Cham: Springer International Publishing), 483
—. 2017b, Thermonuclear Explosions of Chandrasekhar Mass White Dwarfs (Cham: Springer International Publishing), 1275
Nomoto, K., et al. 1982, Nature, 299, 803
Osher, S., & Sethian, J. A. 1988, Journal of Computational Physics, 79, 12
Peter, N. 1999, JPM, 384, 107
Plewa, T. 2007, Astrophys. J., 657, 942
Pocheau, A. 1994, Phys. Rev. E, 49, 1109
Pumo, M. L., et al. 2009, Astrophys. J., 705, L138
Raddi, R., Hollands, M. A., Koester, D., et al. 2018, ApJ, 858, 3
Reinecke, M., Hillebrandt, W., & Niemeyer, J. C. 1999, A&A, 347, 739
—. 2002a, A&A, 386, 936
—. 2002b, A&A, 391, 1167
Röpke, F. K. 2005, A&A, 432, 969
Röpke, F. K., & Hillebrandt, W. 2005, A&A, 431, 635
Röpke, F. K., Hillebrandt, W., & Niemeyer, J. C. 2004a, A&A, 420, 411
—. 2004b, A&A, 421, 783
Röpke, F. K., Hillebrandt, W., Schmidt, W., et al. 2007, ApJ, 668, 1132
Rosswog, S., & Liebendoerfer, M. 2003, Mon. Not. R. astr. Soc., 342, 673
Schmidt, W., Niemeyer, J. C., Hillebrndt, W., & Roepke, F. K. 2006, Astron. Astrophys., 450, 283

Schwab, J., Martinez-Rodriguez, H., Piro, A. L., & Badenes, C. 2017, Astrophys. J., 851, 105
Schwab, J., Quataert, E., & Bildsten, L. 2015, Mon. Not. R. astr. Soc., 453, 1910
Seitenzahl, I. R., Ropeke, F. K., Fink, M., & Pakmor, R. 2010, Mon. Not. R. astr. Soc., 407, 2297
Shen, H., Toki, H., Oyamatsu, K., & Sumiyoshi, K. 1998, Nucl. Phys. A, 637, 435
Siess, L. 2007, Astron. and Astropart., 476, 893
Sugimoto, K., & Nomoto, K. 1980, Space Sci. Rev., 25, 155
Suzuki, T., Toko, H., & Nomoto, K. 2016, Astrophys. J., 817, 163
Takahashi, K., et al. 2013, Astrophys. J., 771, 28
Timmes, F. X. 1999, Astrophys. J., 124, 241
Timmes, F. X., & Arnett, D. 1999, Astrophys. J., 125, 277
Timmes, F. X., & Woosley, S. E. 1992, Astrophys. J., 396, 649
Toki, H., Suzuji, T., Nomoto, K., et al. 2013, Phys. Rev. C, 88, 015806
Townsley, D. M., Calder, A. M., Asida, S. M., et al. 2007, Astrophys. J. Suppl., 143, 201
Wanajo, S., Müller, B., Janka, H.-T., & Heger, A. 2018, ApJ, 852, 40
Wang, R., & Spiteri, R. J. 2007, SIAM J. Numer. Anal., 45, 1871
Woosley, S. E. 1997, ApJ, 476, 801
Woosley, S. E., & Heger, A. 2015, ApJ, 810, 34
Yoon, S.-C., et al. 2007, Mon. Not. R. astr. Soc., 380, 993